Physics of Plasmas

TUTORIAL | MAY 12 2023

# Principles and applications of x-ray light sources driven by laser wakefield acceleration



**Special Collection:** Papers from the 64th Annual Meeting of the APS Division of Plasma Physics , Reviews and Tutorials in Plasma-Based Accelerators, Beams, and Radiation Generation

Félicie Albert



*Phys. Plasmas* 30, 050902 (2023)
https://doi.org/10.1063/5.0142033







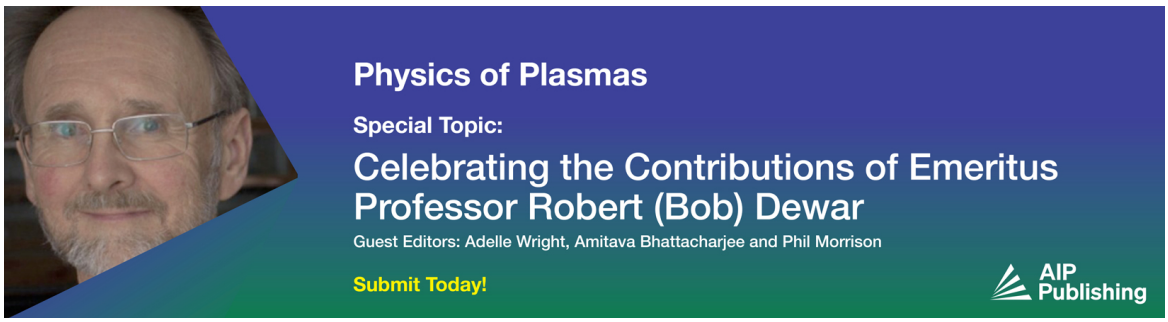

Physics of Plasmas TUTORIAL pubs.aip.org/aip/php

# Principles and applications of x-ray light sources driven by laser wakefield acceleration

Cite as: Phys. Plasmas **30**, 050902 (2023); doi: 10.1063/5.0142033
Submitted: 10 January 2023 · Accepted: 20 April 2023 ·
Published Online: 12 May 2023



Félicie Albert[a),b)]

## AFFILIATIONS

National Ignition Facility and Photon Sciences, Lawrence Livermore National Laboratory, 7000 East Avenue, Livermore, California 94550, USA

**Note:** This paper is part of the Special Collection: Papers from the 64th Annual Meeting of the APS Division of Plasma Physics.
**Note:** Paper PT2 1, Bull. Am. Phys. Soc. 67 (2022).
[a)]Invited speaker
[b)]**Author to whom correspondence should be addressed:** albert6@llnl.gov

## ABSTRACT

One of the most prominent applications of modern particle accelerators is the generation of radiation. In a synchrotron or an x-ray free electron laser (XFEL), high energy electrons oscillating in periodic magnetic structures emit bright x rays. In spite of their scientific appeal that will remain evident for many decades, one limitation of synchrotrons and XFELs is their typical mile-long size and their cost, which often limits access to the broader scientific community. This tutorial reviews the principles and prospects of using plasmas produced by intense lasers as particle accelerators and x-ray light sources, as well as some of the applications they enable. A plasma is an ionized medium that can sustain electrical fields many orders of magnitude higher than that in conventional radio frequency accelerator structures and can be used to accelerate electrons. When short, intense laser pulses are focused into a gas, it produces electron plasma waves in which electrons can be trapped and accelerated to GeV energies. This process, laser-wakefield acceleration (LWFA), is analogous to a surfer being propelled by an ocean wave. Many radiation sources, from THz to gamma-rays, can be produced by these relativistic electrons. This tutorial reviews several LWFA-driven sources in the keV-MeV photon energy range: betatron radiation, inverse Compton scattering, bremsstrahlung radiation, and undulator/XFEL radiation. X rays from laser plasma accelerators have many emerging applications. They can be used in innovative and flexible x-ray imaging and x-ray absorption spectroscopy configurations, for use in biology, industry, and high-energy density science.





## I. INTRODUCTION

Since they were proposed in 1979 by Tajima and Dawson,[1] laser plasma electron accelerators have been extensively studied through theory, simulations, and experiments and have expanded their reach to applications that can span many disciplines, such as medicine, industry, defense, material, and high-energy density sciences.[2] One such application is the production of compact light sources with unique properties,[3] offering alternatives to large synchrotrons and free electron lasers.[4,5]

This tutorial paper reprises many recent results and findings on the subject of x-ray sources driven by laser wakefield acceleration (LWFA) and gives the tools to understand and design such sources for a particular application. The paper is organized as follows: In Sec. II, we review the principles and current status of laser wakefield acceleration, sufficient to provide a good understanding of the electron beam properties that govern the production of light sources; in Sec. III, we present four sources produced by laser wakefield accelerated electrons: betatron radiation, inverse Compton scattering (ICS), bremsstrahlung radiation, and undulator/XFEL radiation. While they can be described using similar formalism, each has a different level of maturity and application space, which we discuss as well. Finally, before concluding and providing open questions, we give an overview of three application techniques in Sec. III, with potential applications in medicine, defense/industry, and high-energy density sciences.

There are many existing reviews of x-ray sources driven by LWFA. Reference 3 presents betatron radiation, ICS, and undulator radiation within a unified formalism, and Refs. 4 and 5 connect these sources to potential applications. Since these reviews have been written, much progress has happened in the field. First, the creation of high power laser networks, such as LaserNetUS,[6] has reinvigorated the

field, and the 2020 roadmap on laser-plasma accelerators[2] cites LWFA-driven light sources as an important application. Second, a LWFA-driven XFEL was demonstrated recently by two groups in the unseeded[7] and seeded[8] regimes. These results are very promising for new applications. Finally, high repetition rate laser technology, coupled with automation, is progressing rapidly,[9] which will help to make LWFA-driven light sources practical and reliable for applications requiring stable beams.[10] An exhaustive description of applications and their connections to the various light sources were given in Ref. 5, and in this new manuscript, Sec. IV focuses on three applications where new results have been published since.

## II. ACCELERATION OF ELECTRONS IN LASER-PRODUCED PLASMAS

LWFA theory and current status have been discussed in many review articles,[2,11] and this section gives an overview of the mechanisms at play to understand electron beam parameters governing light emission. We start with a brief description of the propagation of ultrashort laser pulses in an underdense plasma, nonlinear effects (relativistic self-focusing and the ponderomotive force), the formation of electron plasma waves (the accelerating structure), trapping and acceleration of electrons in electron plasma waves, and finally, light source-relevant regimes of laser plasma acceleration.

### A. Propagation of ultrashort laser pulses in a plasma

Laser light propagation in media is well described with Maxwell's equations; however, some important concepts are relevant to introduce for the particular case of laser pulses needed for laser-plasma acceleration. Chirped pulse amplification, invented by Strickland and Mourou in 1985[12] (and recognized by the 2018 Nobel Prize in Physics), has enabled the production of high-energy ultrashort laser pulses beyond relativistic intensities. A relativistic intensity laser pulse is best described through the laser normalized vector potential $a_0$, which is the ratio between the classical electron velocity under the action of the laser to the speed of light. The equation of motion for an electron of mass $m$ and charge $e$ oscillating in the laser field $\mathbf{E}$, $m\frac{d\mathbf{v}}{dt} = -e\mathbf{E}$, can be solved by assuming that $\mathbf{E} = -\frac{\partial \mathbf{A}}{\partial t}$ and, thus, $\mathbf{v} = \frac{e\mathbf{A}}{m}$. By writing the laser potential $A = A_0 e^{i\phi}$, where $A_0$ is the maximum potential amplitude, and normalizing to the speed of light $c$ yields the expression for the peak amplitude of the laser normalized vector potential $a_0 = eA_0/mc$. For a linearly polarized plane wave, using the expression for the peak laser intensity $I_0 = E_0^2/\mu_0 c$ gives[13]

$$a_0 = \left(\frac{e^2}{2\pi^2\varepsilon_0 m^2 c^5}\lambda^2 I_0\right)^{1/2} = 8.5\times10^{-10}\lambda\,(\mu\mathrm{m})I_0^{1/2}(\mathrm{W/cm^2}). \tag{1}$$

If $a_0 > 1$, we are in a relativistic regime, and for a wavelength $\lambda = 800$ nm (corresponding to a Ti:Sapphire laser system, which is at present the preeminent gain medium used to produce ultrashort pulses), it means a peak intensity $I_0 > 10^{18}$ W/cm$^2$. The intensity of a laser focused onto and propagating into a plasma varies as a function of the radius $r$ with respect to the propagation axis $z$. For a Gaussian beam, the laser waist varies as $w(z) = w_0(1 + (z/z_R)^2)^{1/2}$, where $z_R$ is the Rayleigh length, over which the intensity decreases from half its maximum value. For $\lambda = 1\,\mu$m and a spot size at best focus $w_0 = 20\ \mu$m, $z_R = 1.2$ mm. As long as relativistic intensity can be maintained throughout, a longer Rayleigh length (a longer focal length) is typically preferred for LWFA experiments, where the goal is to accelerate electrons to high energies and/or produce radiation.

Throughout this tutorial, we will always assume that intense laser beams have sufficient intensity to form fully ionized plasmas.[14] LWFA can be realized with different gases, such as hydrogen (full ionization threshold of $I = 1.3\times10^{14}$ W/cm$^2$), or helium (full ionization threshold of $I = 8.76\times10^{15}$ W/cm$^2$.) In this case, the laser, with frequency $\omega_0$ and wavenumber $k$, will propagate in the plasma if its electron density $n_e$ is less than the critical density $n_c$ (underdense regime) such that $\omega_0 = \sqrt{\frac{n_c e^2}{m\varepsilon_0}}$. Then, the pulse propagates and obeys the dispersion relation $\omega_0^2 = \omega_p^2 + k^2c^2$, where $\omega_p = \sqrt{\frac{n_e e^2}{m\varepsilon_0}}$ is the electron plasma frequency, the natural oscillation of electrons in the plasma. The corresponding plasma period is $\lambda_p = 2\pi/\lambda_p$, and the ion plasma frequency $\omega_{pi} = \sqrt{Z\frac{m}{m_i}}\omega_p$. For $n_e = 10^{19}$ cm$^{-3}$, $\omega_p = 1.78\times10^{14}$ s$^{-1}$, $\lambda_p = 10.5\ \mu$m, and $\omega_{pi} \sim 0.03\ \omega_p$. When discussing the formation of a laser plasma accelerator, especially at ultrashort (10's of fs) laser pulse duration, we will generally consider the ions to be immobile.

### B. Nonlinear effects

#### 1. Relativistic self-focusing

As the laser propagates in an underdense plasma, above a certain intensity, the plasma acts as a lens and focuses the laser beam, due to the intensity-dependent nonlinear index of refraction $n = n_0 + n_2 I(r)$, where $n_2$ is the nonlinear index of refraction and $I(r)$ is the laser intensity as a function of the radius (from the laser propagation axis). By definition, the index of refraction is $n = c/v_p = ck/\omega_0$, where $v_p$ is the laser phase velocity. Using the dispersion relation $\omega_0^2 = \omega_p^2 + k^2c^2$, the index of refraction of the plasma is then

$$\sqrt{1-\frac{\omega_p^2}{\omega_0^2}} \sim 1 - \frac{\omega_p^2}{2\omega_0^2}. \tag{2}$$

Due to their transverse oscillations in the laser field, electrons experience a relativistic mass change and their mass is $m\gamma_\perp$, where $\gamma_\perp = (1+\frac{a_0^2}{2})^{1/2}$. Thus, the effective plasma frequency is now $\omega_p/\sqrt{\gamma_\perp}$, and we can re-write the index of refraction as[15] $n = 1 - \frac{ne}{2\gamma_\perp n_c}$. By taking the part that depends on the intensity, we get $n_2 = \frac{2n_e}{n_c a_0^2}$, and for a Gaussian beam [Eq. (1)], we deduce the threshold laser power for the $n_2$ contribution to the index of refraction to be significant such as

$$P_c = \frac{8\pi\varepsilon_0 m_e^2 c^5}{e^2}\frac{n_c}{n_e} = 17.4\frac{n_c}{n_e}(\mathrm{GW}). \tag{3}$$

$P_c$ is the threshold power for relativistic self-focusing. For $n_e = 10^{19}$ cm$^{-3}$ and $\lambda = 800$ nm, $P_c = 2$ TW. Most modern high intensity laser facilities are one or more orders of magnitude above this threshold.

#### 2. Ponderomotive force

When a high intensity laser pulse propagates in an underdense plasma, light pressure becomes significant.[16,17] The corresponding

ponderomotive force $\mathbf{F_p}$ can be derived from the equation of motion of an electron oscillating in the laser fields $\mathbf{E}$ and $\mathbf{B}$: $m\frac{dv}{dt} = -e(\mathbf{E} + v \times \mathbf{B})$. Here, we use the plasma fluid description, and the electron velocity $v = v(x, y, z, t)$ is a property of the fluid element (a small quantity of fluid that contains the same material at all times as the fluid moves). During a small-time $dt$, the fluid quantities change: $(x, y, z) \rightarrow (x + dx, y + dy, z + dz)$ and $v \rightarrow v + dv$, where $dv = \frac{\partial v}{\partial t}dt + \frac{\partial v}{\partial x}dx + \frac{\partial v}{\partial y}dy + \frac{\partial v}{\partial z}dz$. Hence, $\frac{dv}{dt} = \frac{\partial v}{\partial t} + \left(\frac{\partial}{\partial x}\frac{dx}{dt} + \frac{\partial}{\partial y}\frac{dy}{dt} + \frac{\partial}{\partial z}\frac{dz}{dt}\right)\mathbf{v} = \frac{\partial v}{\partial t} + (\mathbf{v}.\nabla)\mathbf{v}$, and the plasma fluid equation of motion is

$$\frac{\partial v}{\partial t} + (\mathbf{v}.\nabla)\mathbf{v} = -\frac{e}{m}(\mathbf{E} + \mathbf{v} \times \mathbf{B}). \tag{4}$$

It can be decomposed into first (linear response) and second (nonlinear response) orders. In the first order, it is the equation of motion of an electron oscillating in a laser field $\frac{\partial v_L}{\partial t} = -\frac{e}{m}\mathbf{E}$. By taking $\mathbf{E} = \mathbf{E_0}\cos(\omega_0 t - kz)$, then the linear electron velocity is

$$v_L = -\frac{e}{m\omega_0}E_0 \sin(\omega_0 t - kz). \tag{5}$$

In the second order, the equation of motion is

$$m\frac{\partial v_{NL}}{\partial t} = (\mathbf{v}.\nabla)\mathbf{v} - e(\mathbf{E} + \mathbf{v} \times \mathbf{B}). \tag{6}$$

The right-hand side can be re-written by considering $v \sim v_L$ (weakly relativistic case), which means that $(\mathbf{v}.\nabla)\mathbf{v} \sim \frac{e^2}{m\omega_0^2}(\mathbf{E_0}.\nabla)\mathbf{E_0}\mathbf{sin^2}(\boldsymbol{\omega_0 t} - \mathbf{kz})$, and by solving Maxwell's equation $\nabla \times \mathbf{E} = -\frac{\partial \mathbf{B}}{\partial t}$, we obtain $\mathbf{B} = -\frac{1}{\omega_0}\nabla \mathbf{E_0}\sin(\omega_0 t - kz)$ and $-e(\mathbf{E} + \mathbf{v} \times \mathbf{B}) = -\frac{e^2}{m\omega_0^2}\mathbf{E_0} \times (\nabla \times \mathbf{E_0})sin^2(\omega_0 t - kz)$. If we average over one laser period, then $m\frac{\partial \langle v_{NL}\rangle}{\partial t} = -\frac{e^2}{m\omega_0^2}((\mathbf{E_0}.\nabla)\mathbf{E_0} + \mathbf{E_0} \times (\nabla \times \mathbf{E_0}))$, which can be solved with a vector identity to obtain

$$m\frac{\partial \mathbf{V_{NL}}}{\partial t} = \mathbf{F_p} = -\frac{e^2}{4m\omega_0^2}\nabla \mathbf{E_0^2}. \tag{7}$$

We can immediately see that the ponderomotive force, $\mathbf{F_p}$, is inversely proportional to the gradient of light intensity and will tend to push the electrons away from the strong field regions, separating ions, and electrons, as shown in Fig. 1. Just like any conservative force, it derives from a potential, such as $\mathbf{F_p} = -\nabla.\Phi_p$, where $\Phi_p = I/2cn_c$ is the ponderomotive potential. For a laser intensity $I = 3 \times 10^{18}$ W/cm$^2$ and $\lambda = 800$ nm, then $\Phi_p = 0.2$ MeV. This numerical example shows that while the ponderomotive force separates electrons from ions and initiates the creation of electron plasma waves by inducing electron density perturbations, it is not sufficient to explain acceleration of electrons to GeV-class energies.

### C. Electron plasma waves

Here, we start with a simple, one-dimensional, non-relativistic description of an electron plasma wave and its associated electrical field, like in Tajima and Dawson.[1] In a plasma, the longitudinal electron density perturbation $\delta n_e$ can be expressed as

$$\frac{\delta n_e}{n_e} = \delta \sin(k_p z - \omega_p t), \tag{8}$$

where $0 < \delta < 1$. To calculate the corresponding field, we use Poisson's equation $\nabla.\mathbf{E} = \frac{\rho}{\varepsilon_0}$, and integrate to obtain an expression for the electrical field $E(z, t) = \frac{en_e c\delta}{\varepsilon_0 \omega_p}$, as shown in Fig. 1. The maximum amplitude of the electrical field in this simple case is the cold nonrelativistic wavebreaking limit,

$$E_{\max} = \frac{m_e c\omega_p}{e}. \tag{9}$$

For an electron density $n_e = 10^{18}$ cm$^{-3}$, $E_{max} = 96$ GV/m, which is about three orders of magnitude larger than in a conventional RF particle accelerator. Realistically, in laser wakefield acceleration, electron plasma waves are relativistic and three-dimensional. An electron plasma wave is in fact a longitudinal Langmuir wave, which obeys the dispersion relation $\omega_{pe}^2 = \omega_p^2 + 3k_p^2 v_{th}^2$. For a cold plasma, $v_{th} = 0$ and, thus, $k_p = \omega_p/v_p$. If $v_p \sim c$, the plasma wave is relativistic and the plasma wave relativistic factor is $\gamma_p = \left(1 - \frac{v_p^2}{c^2}\right)^{-1/2}$. The plasma wave phase velocity moves with the laser group velocity, and, thus, relativistic plasma wave excitation is more efficient if the resonance condition $c\tau \sim \lambda_p/2$ is satisfied. For $n_e = 10^{18}$ cm$^{-3}$, the plasma period is $\lambda_p = 33$ $\mu$m and, thus, $\tau = 110$ fs, which means that ultrashort pulses are more efficient to excite relativistic electron plasma waves. For a linear three-dimensional electron plasma wave, the fields can be calculated by using the plasma fluid equations and Poisson's equation. For a nonlinear case, the electrical field can go beyond the cold wavebreaking limit. In one dimension, the fields are solved by using quasi-static approximations, where the drive beam and plasma fluid quantities are a function only of a co-moving variable $\xi = z - v_p t$. As the laser envelope varies slowly, we can neglect time derivatives in equations. A

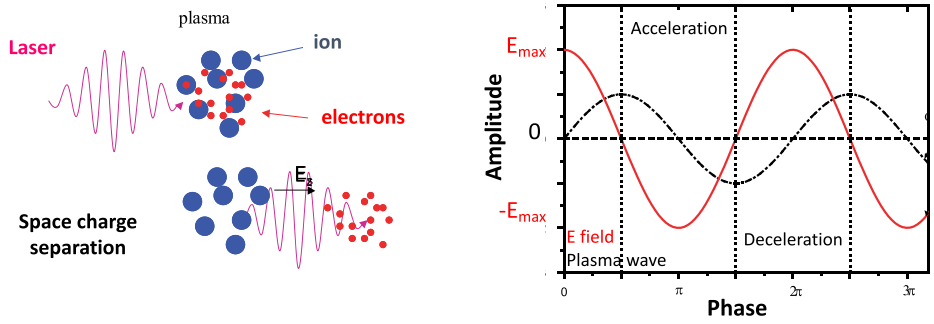


**FIG. 1.** Illustration of the ponderomotive force creating a longitudinal density perturbation and electrical field $E_z$. The field, represented in 1D, has an amplitude $E_{max}$ and accelerating/decelerating phases.

nonlinear three-dimensional case requires extensive calculations, using nonlinear plasma fluid models, nonlinear quasistatic fluid models, or particle-in-cell (PIC) simulations.

### D. Trapping of electrons in electron plasma waves

Before being accelerated, electrons first have to be trapped into the electron plasma wave. By definition, trapping of an electron into a LWFA occurs when the electron has gained enough energy from the wakefield to move at the phase velocity $v_p$ of the wakefield. The trapping mechanism of electrons into a plasma wave is often illustrated by a surfer trying to catch a wave: A surfer not paddling will not catch it. The trapping of electrons into a wakefield can be studied theoretically using a 3D Hamiltonian description of an electron within an electromagnetic field.[11] In this description, a constant of motion can be found, which relates the scalar and vector potentials of the wake and laser to the momentum of an electron. In this manner, the required potential difference that an electron must experience to become trapped can be solved for. The minimum and maximum energies required for an electron to be trapped into the plasma wave can, thus, be calculated by calculating its energy conservation (kinetic and potential energy), first in the plasma wave reference frame. In the laboratory frame, the minimum and maximum the electron relativistic factor must satisfy for trapping are[18]

$$\gamma_{\min} = \gamma_p(1 + 2\gamma_p\delta) - \sqrt{\gamma_p^2 - 1}\sqrt{(1 + 2\gamma_p\delta)^2) - 1} \quad (10)$$

and

$$\gamma_{\max} = \gamma_p(1 + 2\gamma_p\delta) + \sqrt{\gamma_p^2 - 1}\sqrt{(1 + 2\gamma_p\delta)^2) - 1}. \quad (11)$$

For a density perturbation with maximum amplitude $\delta \sim 0.05$ and a plasma wave with relativistic factor $\gamma_p = 10$, then an electron will be trapped if its initial energy is between 1.5 and 18.5 MeV. Understanding the injection and trapping of electrons is important for creating high quality, reproducible electrons beams necessary for use in light sources. Electrons can either be externally injected from an electron beam source into the LWFA, or they can be injected from the background plasma into the LWFA, which is easier than external injection. A non-exhaustive list of the techniques and mechanisms (in both the linear and quasi-linear regimes) used to inject electrons includes self-injection, ionization injection,[19,20] colliding-pulse injection,[21] downramp injection,[22] and shock-assisted injection.[23] Self-injection happens when a strong wake is driven and a large electron density spike forms at the back of the first period of the wakefield. As electrons are drawn back to the end of the plasma period, this density spike deflects some of the electrons and injects them into the large longitudinal electric field at the back of the wake, where they are quickly accelerated by the wakefield to the phase velocity of the wake. These electrons are, thus, trapped and continue to gain further energy from the wakefield. There is a minimum electron density threshold for trapping to occur, and due to the nonlinear nature of this process, the final electron beam properties can be more difficult to control. However, it has the potential to produce short (and monoenergetic) electron bunches. In ionization injection, trace amounts of dopant gas (typically nitrogen) are added so that it can be ionized only near the laser intensity peak, directly inside the first plasma wave period. Since electrons are trapped near the peak of the laser intensity, this produces continuous injection and, thus, larger energy spreads, but the electron density threshold is lower than for self-injection. It also produces higher charge electron beams, which is good for increasing the flux of light sources. In colliding-pulse injection, a quasi-counterpropagating laser pulse interacts with the drive laser pulse to create a beat pattern, heating the electrons so that they can gain momentum and be trapped in the plasma wave at a precise and controlled location. This technique ensures exquisite control of the energy and energy spread of the electrons.

### E. Limitations to electron energy gain

Three main characteristic lengths can limit the electron energy gain in laser wakefield acceleration: diffraction, dephasing, and depletion lengths. When designing a light source, it is important to keep them in mind. The diffraction length is simply the length over which the laser stays focused to maintain sufficient intensity. It is usually no more than a few Rayleigh lengths, which is why a soft focus is better.

The dephasing length is the length over which the electrons catch up with the wave so that they are no longer in an accelerating field and start to decelerate (see Fig. 1). As electrons are accelerated, their velocity increases to approach the speed of light. The plasma wave travels with a phase velocity $v_p$, which is close to the laser group velocity and $<c$. Eventually, the electrons outrun the plasma wave and dephase. If we define the dephasing length $L_d$ as the length the electron must travel to slip by 1/2 period with respect to the plasma wave, then $k_p(L_d - v_p t) = \pi$. With the electron velocity close to the speed of light, then the cold, 1D limit for the dephasing length is $L_d = \lambda_p/2(1 - v_p/c) \sim \gamma_p^2\lambda_p$. For $n_e = 10^{18}$ cm$^{-3}$ ($\lambda_p = 33$ $\mu$m), and $\gamma_p = 10$, then $L_d = 3.3$ mm. An ideal laser wakefield accelerator is when the acceleration length is equal to the dephasing length, and, thus, energy gain will be $\delta E_\gamma = eE_{\max}L_d$. In 3D, the dephasing length expression takes into account the transverse dimensions of the plasma wave (dictated by the laser focusing geometry).[24] A current active area of research, which is very promising for optimizing LWFA-driven light sources even at the potential cost of laser energy, is the design of dephasingless laser wakefield accelerators,[25] enabled by the use of a flying focus.[26]

As electrons are accelerated, the laser transmits energy to the plasma wave until it is depleted. The pump depletion length $L_{pd}$ is calculated by equating the laser pulse energy to the energy left in the wakefield $E_z^2 L_{pd} = E_L^2 c\tau$, where $E_z$ and $E_L$ and the electrical fields for the wakefield and laser, respectively. We consider that the resonance condition in the 1D limit $c\tau = \lambda_p/2$ is satisfied. For the laser field, we consider $\mathbf{E} = \frac{\partial \mathbf{A}}{\partial t}$, and using the definition of the laser normalized potential, we get the expression $E_l = \frac{m_e c\omega_0 a_0}{e}$. For a Gaussian laser pulse, $a^2 = a_0^2 e^{-\left(\frac{z-ct}{c\tau}\right)^2}$ and, thus, $E_z = E_{\max}\left(\sqrt{\pi}\frac{a_0^2}{2}\right)k_p c\tau e^{-\left(\frac{k_p c\tau}{2}\right)^2}$, we get, in the linear regime, $L_{pd} \sim \lambda_p^3/2a_0^2\lambda^2$. For $n_e = 10^{18}$ cm$^{-3}$ ($\lambda_p = 33$ $\mu$m) and $a_0 = 0.3$, then $L_{pd} = 2.8$ cm.

### F. Light source-relevant regimes of laser wakefield acceleration

Since the work of Tajima and Dawson,[1] many laser wakefield acceleration schemes have been studied, mainly due to the rapid progress in laser technology and large scale computer simulations. A regime is dictated by the interplay between laser intensity, pulse length,

spatial dimensions, and electron density. A description of each of them can be found in the literature,[11] and the main regimes in which light sources have been developed are described here.

#### 1. Blowout regime

The blowout regime is a highly nonlinear, 3D regime[27,28] in which quasi-monoenergetic electron beams can be accelerated to GeV-class energies. It was a notable advance in the field when three groups independently demonstrated this process, leading the research to be featured on the cover of *Nature* as the "Dream Beam."[29–31] Betatron radiation from LWFA was also first reported at this time,[32] realized in the blowout regime. Here, the plasma period must be greater than the laser pulse length. If the laser intensity is sufficiently high, the ponderomotive force completely expels the electrons away from the high intensity regions, which forms an ion cavity in the wake of the laser pulse. The electron density, laser spot size, and duration must be chosen so that the radius of the bubble $R$ is matched to the laser longitudinal and transverse dimensions. For $2 < a_0 < 4$, a series of scaling laws have been established,[27] benchmarked against large 3D PIC simulations and many experiments. The dephasing length and pump depletion length are, respectively, $L_d = \frac{2}{3}\frac{n_c}{n_e}R$ and $L_{dp} = \frac{n_c}{n_e}c\tau$. The electron energy gain is then expressed as a function of the laser and plasma parameters:

$$\Delta E(\mathrm{GeV}) = 1.7\left(\frac{P(\mathrm{TW})}{100}\right)^{1/3}\left(\frac{10^{18}}{n_e(\mathrm{cm}^{-3})}\right)^{2/3}\left(\frac{0.8}{\lambda(\mu\mathrm{m})}\right)^{4/3}. \quad (12)$$

#### 2. Self-modulated regime

In self-modulated laser wakefield acceleration (SMLWFA), the laser pulse is several plasma periods in length. This regime has been widely studied in the 1990s[33] for laser pulse lengths on the order of a picosecond, before high intensity femtosecond lasers became available. Betatron radiation in this regime was first reported in 2008[34] for intensities above $10^{20}$ W/cm$^2$ and then in 2017[35] for lower intensities.

In SMLWFA, the electron plasma wave is excited by the self-modulation and Raman forward instabilities.[36] The Raman forward instability occurs when an electromagnetic wave with frequency $\omega_0$ (the laser) is decomposed into a plasma wave with frequency $\omega_p$ and scattered wave with frequency $\omega_s$ such that $\omega_0 = \omega_p - \omega_s$. While this process can be detrimental in inertial confinement fusion (ICF) experiments (it reduces the coupling between the laser and the target and can send laser light back into the system), it can excite very large amplitude electron plasma waves. It is initiated when the laser ponderomotive force creates a density perturbation at the plasma frequency $\omega_p$. The backscattered wave with frequency $\omega_s$ propagates in the opposite direction to that of the incident laser pulse, which creates a beat-wave pattern of the laser envelope at $\omega_p$. This modulated envelope then resonantly interacts with the plasma wave, which in turn increases its amplitude. When it reaches the wavebreaking limit, electrons can be trapped and accelerated into the plasma wave. Because electrons are trapped into multiple plasma wave periods, unlike the blowout regime, the spectrum is characterized by a Maxwellian distribution. As the laser pulse is typically longer than in the blowout regime, the plasma can get hotter, which reduces the theoretical wavebreaking limit and, thus, the maximum electron energy. Due to the growth rate of the Raman instability, SMLWFA is also better suited for picosecond-scale pulses.

## III. X-RAY LIGHT SOURCES

In this section, we review the four main mechanisms producing x rays in the keV–MeV energy range with LWFA electrons, and the properties of the photons they emit. For Betatron, undulator, and inverse Compton scattering radiation, the process is very similar and can be parametrized[3] because the spectrum is that of a relativistic electron undergoing oscillations. These oscillations are, respectively, induced by space-charge separation in the wakefield, an externally applied magnetic field, and by a laser field. A schematic representation of the four light sources is shown in Fig. 2.

### A. Betatron

Betatron oscillations naturally occur for electrons accelerated in the wake of the laser pulse.[37] If an electron is injected off the laser propagation axis, it experiences a transverse restoring force that can be calculated with Gauss' law,

$$\mathbf{F} = -m_e\omega_p\frac{\mathbf{r}}{2}; \quad (13)$$

hence, the equation of motion for the electron is governed by the transverse and longitudinal forces,

$$\frac{d\mathbf{p}}{dt} = -m_e\omega_p\frac{\mathbf{r}}{2} - \alpha e\mathbf{E_z}. \quad (14)$$

In the blowout 3D nonlinear regime of laser wakefield acceleration,[27] $\alpha = \frac{1}{2}\sqrt{a_0}$ is the normalized accelerating field. If we neglect acceleration, the equation is that of a harmonic oscillator,

$$\frac{d^2x}{d^2t} = \frac{\omega_p^2}{2\gamma}x, \quad (15)$$

where the electron transverse position $x = r_0\sin(\omega_\beta t)$ is defined as a function of the betatron frequency $\omega_\beta = \omega_p/\sqrt{2\gamma} = 2\pi c/\lambda_\beta$, where $\lambda_\beta$ is the betatron period and $r_0$ is the betatron oscillation radius at the time of injection (see Fig. 2). For $n_e = 10^{19}$ cm$^{-3}$ and $\gamma = 200$, the betatron period is $\lambda_\beta = 212$ $\mu$m. In synchrotrons and XFELs, the magnetic undulator period is typically on the order of a centimeter. If we approximate that the longitudinal velocity of the electrons is the speed of light ($z = ct$), then we can express the particle transverse position as a function of its longitudinal position $x = r_0\sin(k_\beta z)$. The angular excursion of the electron with respect to the propagation axis is then $\theta = (\frac{dx}{dz})_{z=0} = k_\beta r_0$. We can then define the betatron wiggler strength $K_u = \gamma_\theta = \gamma k_\beta r_0$, which, in practical units, is

$$K_u = 1.33\times10^{-10}\sqrt{\gamma n_e(\mathrm{cm}^{-3})}r_0(\mu\mathrm{m}). \quad (16)$$

In laser plasma acceleration, betatron oscillations typically produce fundamental radiation in the soft x-ray regime. A relativistic electron undergoing oscillations with a period $\lambda_\beta$ emits at a wavelength of $\lambda_\beta/2\gamma^2$ (first due to the Lorentz transform of the electron trajectory from the laboratory frame to its own frame, and then to the Doppler effect when observing the electron dipole emission pattern emitted in its own frame back in the laboratory frame of reference). In reality, $z \sim ct$ is only an approximation, and one need to take into account both the longitudinal and transverse components of the electron

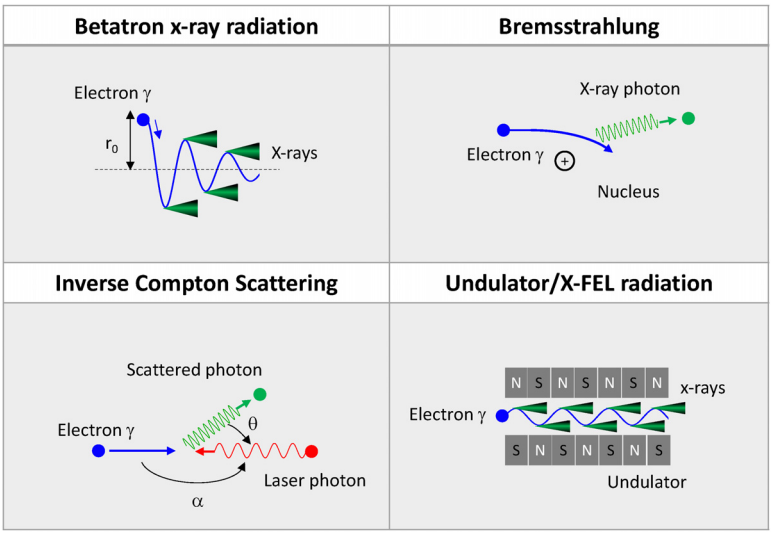


**FIG. 2.** Schematic representation of x-ray sources driven by laser wakefield acceleration discussed in this tutorial.

velocity when solving the equation of motion such that $\gamma = \sqrt{\frac{1}{1-\beta^2}} = \sqrt{\frac{1}{1-\beta_z^2-\beta_x^2}}$. This results in coupling between the transverse and longitudinal components of the position and velocity, producing harmonics. Solving for the second order, the position and velocity are[37]

$$z = \left(1 - \frac{1}{2\gamma^2} - \frac{k_\beta^2 r_0^2}{4}\right)ct - \frac{k_\beta^2 r_0^2}{8}\sin(2k_\beta ct) \tag{17}$$

and

$$\beta_z = 1 - \frac{1}{2\gamma^2} - \frac{k_\beta^2 r_0^2}{4} - \frac{k_\beta^2 r_0^2}{4}\cos(2k_\beta ct). \tag{18}$$

Then, the emission will contain harmonics of the fundamental radiation frequency such as

$$\omega_n = \frac{2\gamma^2 n\omega_\beta}{1 + K_u^2/2}. \tag{19}$$

The detailed calculation of the radiation emitted by a moving electron has been presented in many references[38] and was introduced in a publication by Larmor[39] for non-relativistic electrons, then extended to arbitrary velocities in 1898 by Liénard.[40] A detailed calculation of synchrotron radiation was first published by Schwinger in 1949.[41] For a relativistic electron undergoing betatron oscillations in a laser-driven electron plasma wave where $K_u \gg 1$, the radiation is synchrotron radiation from a relativistic particle undergoing instantaneous circular motion. In this case, the radiated power is expressed as

$$P = \frac{2}{3}\frac{e^2 c}{\rho^2}\beta^4\gamma^4, \tag{20}$$

where the trajectory radius of curvature is $\rho = 1/r_0 k_\beta^2$ for betatron oscillations. For a given curvature, the total energy loss per revolution $\delta E = \frac{2\pi\rho}{c\beta}P$ can give an estimate of the spectral range. In more practical units, $\delta E = 8.85 \times 10^{-11}\frac{E(\mathrm{MeV})^4}{\rho(\mathrm{m})}$. Using our previous numerical example ($n_e = 10^{19}$ cm$^{-3}$, $\gamma = 200$ and $r_0 = 1$ $\mu$m), the energy loss is about 7.5 keV. For relativistic motion, this radiated energy is spread over a wide range of frequencies. A detailed derivation can be found in the literature,[38] and here, we present the most important result, the energy radiated per unit frequency $\omega$, and solid angle $\Omega$,

$$\frac{d^2 I}{d\Omega d\omega} = \frac{e^2\omega^2}{4\pi c}\left|\int_{-\infty}^{\infty}\vec{n}\times\left(\vec{n}\times\vec{\beta}\right)e^{i\omega\left(t-\frac{\vec{n}.\vec{r}}{c}\right)}dt\right|^2, \tag{21}$$

where $\vec{n}$ is the vector corresponding to the direction of observation and $\beta = v/c$ is the normalized electron velocity. For relativistic energies, $\beta \sim 1$. In the case where the wiggler parameter $K_u = 1.33 \times 10^{-10}\sqrt{\gamma n_e} r_0$ is larger than unity, the spectrum, observed at an angle $\theta$ from the plane in which the particle oscillates, can be approximated by an asymptotic limit.[37,38] For this, we can consider a coordinate system $(\vec{x}, \vec{y}, \vec{z})$ in which the electron trajectory is contained in the plan formed by $(\vec{x}, \vec{y})$ and the direction of observation $\vec{n}$, at a small angle $\theta$ with respect to the $\vec{x}$ axis. By choosing unit vectors $\vec{\varepsilon}_{||}$ along $\vec{y}$ and $\vec{\varepsilon}_\perp$ such that $\vec{\varepsilon}_\perp = \vec{n}\times\vec{\varepsilon}_{||}$, then

$$\vec{n}\times\left(\vec{n}\times\vec{\beta}\right) = \beta\left[-\vec{\varepsilon}_{||}\sin\left(\frac{vt}{\rho}\right) + \vec{\varepsilon}_\perp\cos\left(\frac{vt}{\rho}\right)\sin\theta\right] \tag{22}$$

and

$$\begin{aligned}\omega\left(t - \frac{\vec{n}.\vec{r}}{c}\right) &= \omega\left[t - \frac{\rho}{c}\sin\left(\frac{vt}{\rho}\right)\cos\theta\right] \\ &\simeq \frac{\omega}{2}\left[\left(\frac{1}{\gamma^2} + \theta^2\right)t + \frac{c^2}{3\rho^2}t^3\right].\end{aligned} \tag{23}$$

Hence, Eq. (21) becomes

$$\frac{d^2 I}{d\Omega d\omega} = \frac{e^2}{4\pi^2 c}\left|-\vec{\varepsilon}_{||}A_{||}(\omega) + \vec{\varepsilon}_\perp A_\perp(\omega)\right|^2 \tag{24}$$

with

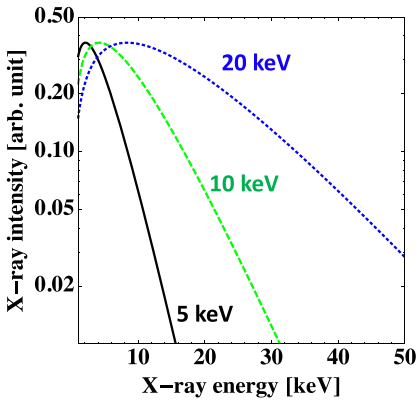


**FIG. 3.** Illustration of Eq. (27), for $\theta = 0$, which corresponds to on-axis radiation, and for several critical energies.

$$A_{||}(\omega) = \frac{c}{\rho}\int_{-\infty}^{\infty} t \exp\left(i\frac{\omega}{2}\left[\left(\frac{1}{\gamma^2}+\theta^2\right)t + \frac{c^2}{3\rho^2}t^3\right]\right)dt \tag{25}$$

and

$$A_{\perp}(\omega) = \theta\int_{-\infty}^{\infty} \exp\left(i\frac{\omega}{2}\left[\left(\frac{1}{\gamma^2}+\theta^2\right)t + \frac{c^2}{3\rho^2}t^3\right]\right)dt, \tag{26}$$

which yields the asymptotic limit:

$$\frac{d^2I}{d\Omega d\omega} = \frac{e^2}{3\pi^2 c}\left(\frac{\omega\rho}{c}\right)^2\left(\frac{1}{\gamma^2}+\theta^2\right)\left[K_{2/3}^2(\xi) + \frac{\theta^2}{(1/\gamma^2)+\theta^2}K_{1/3}^2(\xi)\right], \tag{27}$$

where $K_{2/3}$ and $K_{1/3}$ are modified Bessel functions of the second kind. Here, $\rho$ is the radius of curvature of the electron trajectory and $\xi = \frac{\omega\rho}{3c}\left(\frac{1}{\gamma^2}+\theta^2\right)^{3/2}$. This derivation allows us to introduce an important parameter, $\omega_c = 3\gamma^3 c/\rho$, which is the critical frequency (the frequency below which half of the x-ray source power is radiated). Equation (27) is illustrated for different critical energies $E_c = \hbar\omega_c$ in Fig. 3, for the particular case $\theta = 0$ (observation on axis).

When integrated over all angles of observation, the spectrum becomes

$$\frac{dI}{d\omega} = \sqrt{3}\frac{e^2}{c}\gamma\frac{\omega}{\omega_c}\int_{\frac{\omega}{\omega_c}}^{\infty} K_{5/3}(x)dx, \tag{28}$$

where $K_{5/3}$ is also a modified Bessel function. Equation (27) peaks at $\omega \sim 0.45\omega_c$ for $\theta = 0$ while Eq. (28) peaks at $\omega \sim 0.3\omega_c$. When designing a betatron x-ray source, the critical energy $E_c$ can be rewritten in practical units:

$$E_c(\text{eV}) = 5.21\times10^{-21}\gamma^2 n_e(\text{cm}^{-3})r_0(\mu\text{m}). \tag{29}$$

To calculate the emitted number of photons, one can first determine the total energy radiated by an electron while it oscillates in the wiggler as

$$E = \frac{2e^2}{3}\frac{\gamma^4 N_0\lambda_\beta}{\rho^2}, \tag{30}$$

where we have multiplied the radiated power [Eq. (20) with $\beta = 1$] by the time $T = N_0\lambda_\beta/c$ it takes the electron to oscillate in the wiggler. Then, the number of photons is the radiated energy divided by the mean photon energy [which, for a synchrotron spectrum described by Eq. (28), is $E_{mean} = (8/15\sqrt{3})E_c \sim 0.3E_c$],

$$N_x = \frac{5\sqrt{3}\pi}{6}\frac{e^2}{\hbar c}N_0K_u \sim 3.3\times10^{-2}N_0K_u, \tag{31}$$

where $N_0$ is the number of oscillations undergone by the electron.

There are several methods to simulate betatron radiation spectra and beam profiles. The first one is to use single electron models, which is very useful when trying to design a betatron x-ray experiment. Equation (14) can be solved by using a fourth-order Runge–Kutta algorithm to obtain the single electron trajectories for given initial conditions and fields.[42,43] The electron trajectory is then used to calculate the intensity radiated by the particle per unit frequency $\omega$ and solid angle $\Omega$ with Eq. (21). Similarly, the betatron x-ray beam profile is calculated by integrating Eq. (21) over frequencies. Figure 4 shows an example of electron trajectory, with its corresponding betatron x-ray spectrum and beam profile. For this particular case, the parameters are $n_e = 10^{19}$ cm$^{-3}$, $\gamma = 200$, $x_0 = 1\,\mu$m, $y_0 = 0$, and $\alpha = 0$. The trajectory was calculated using 3000 time steps (with each unit step $dt = 0.2c/\omega_p$). At each point of calculation of the trajectory, the spectrum and beam profile were calculated using frequency steps of 100 eV. For the chosen parameters, $\omega_c = 4.2$ keV and $K_u \simeq 6$. The beam has a divergence of $1/\gamma$ and $K_u/\gamma$ along the direction parallel and perpendicular to the plane of the oscillations, and the on-axis

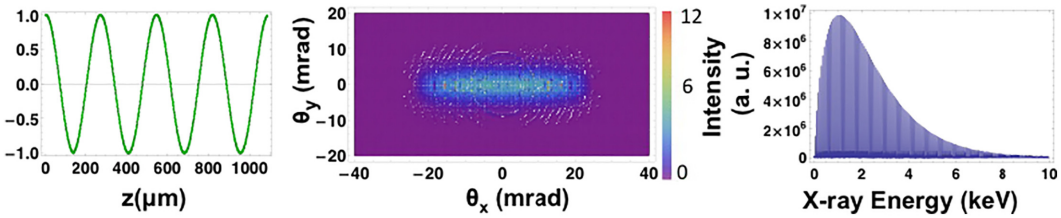


**FIG. 4.** From left to right: example of an electron trajectory in the plasma calculated with a fourth order Runge–Kutta algorithm, with the corresponding betatron x-ray beam profile and spectrum observed on-axis. Shown on the right plot is the full spectrum (solid line), calculated using Eq. (21) and containing the harmonic structure of the radiation. The asymptotic limit, calculated using Eq. (27), corresponds to the envelope of this curve. For this example, the parameters are $n_e = 10^{19}$ cm$^{-3}$, $\gamma = 200$, $x_0 = 1\,\mu$m, $y_0 = 0$, and $\alpha = 0$. Here, the critical frequency $E_c$ (keV) $= 5\times10^{-24}\times\gamma^2 n_e$ (cm$^{-3}$)$r$ ($\mu$m) $= 4.2$ keV and $K_u \simeq 6$. The beam has a divergence of $1/\gamma$ and $K_u/\gamma$ along the direction parallel and perpendicular to the plane of the oscillations.

spectrum peaks at ~2 keV. Although more computationally intensive, the other method uses electrons trajectories obtained from PIC simulations and post-processes them using Eq. (21) to calculate the spectrum and profile with a much better resolution.[44] This is usually better for the self-modulated regime, where trajectories are more complex.[35]

### B. Inverse Compton scattering

Compton scattering occurs when an electromagnetic wave scatters off of a charged particle, in this case, an electron.[45] Because of the wave-particle duality of light, its complete description requires using quantum electrodynamics. Compton scattering refers to the scattering of a photon with energy $E_0$ and momentum $E_0/c$ off of an electron at rest with energy $mc^2$. If the energy transmitted to the electron is $\ll E_0$, then the process can be described with classical electrodynamics and is referred to as Thomson scattering. Since the electron is at rest, the scattered photon energy is less than the incident photon energy. However, in a LWFA, the electron is initially not at rest and is relativistic, typically in a quasi-counter-propagating geometry with respect to the incident laser pulse, and the scattered photon energy is, thus, higher than the incident photon energy. The idea of using relativistic electrons to obtain high energy photons via Compton Scattering was originally proposed by Arutyunian in 1963.[46] In this case, the process is often referred to as Inverse Compton Scattering (ICS), even though it is the same principle if one considers it from the electron reference frame. In LWFA-driven ICS, the scattered photon energy is orders of magnitude higher than the laser photon energy. This is explained by a double Doppler effect. For an electron with relativistic factor $\gamma$, the laser frequency in the electron reference frame is $\omega_0' = 2\gamma\omega_0$ (first Doppler effect). The fundamental radiation frequency emitted by the electron will, thus, be $\omega_0'$ in its reference frame and $2\gamma\omega_0' = 4\gamma^2\omega_0$ in the laboratory reference frame (second Doppler effect). A detailed calculation of the scattered photon energy relies on energy and momentum conservation. Very good descriptions of ICS can be found in the literature for both the case of linac-based electron beams[47] and LWFA-based electron beams.[48] The calculation of the scattered photon energy is done by equating the total energy (momentum) of the particle and the photon before interaction to the total energy (momentum) of the particle and the photon after interaction. For an electron initially at rest (with energy $mc^2$ and momentum 0) and an incident photon with energy $E_0$ (momentum $E_0/c$), the scattered photon energy $E_x$ is

$$E_x = \frac{1}{1+\frac{E_0}{mc^2}(1-\cos\theta)}E_0 = \frac{1}{1+\frac{\lambda_c}{\lambda_0}(1-\cos\theta)}E_0, \tag{32}$$

where $\theta$ is the angle at which the photon is emitted with respect to the laser propagation axis and $\lambda_c = h/mc \sim 2.426\times10^{-12}$ m is the Compton wavelength. If the electron is initially relativistic with normalized velocity $\beta$ and relativistic factor $\gamma$ and makes and angle $\alpha$ with respect to the laser beam propagation axis, then energy-momentum conservation yields

$$E_x = \frac{1+\beta\cos\alpha}{1-\beta\cos\theta+\frac{\gamma\lambda_c}{\lambda_0}(1+\cos(\alpha-\theta))}E_0. \tag{33}$$

By using $\gamma = \sqrt{1/(1-\beta^2)}$, for a head-on collision ($\alpha = 180°$) and observation close to on-axis $\theta \sim 0$ and $\cos\theta \sim 1-\theta^2/2$, then $E_L \sim 4\gamma^2E_0/(1+\theta^2\gamma^2)$. For an ICS source driven by laser wakefield acceleration, there are two important aspects to note. First, the recoil $\gamma\lambda_c/\lambda_0$ (for $\alpha = 180°$ and $\theta = 0$) cannot be neglected if the electron energy is approaching GeV energies. Second, the fact that the electron undergoes transverse oscillations in the laser field reduces its velocity and total relativistic factor $\gamma \to \gamma/\sqrt{1+a_0^2}$. Hence, a more accurate expression for the inverse Compton scattered energy observed close to the axis in LWFA-driven sources is

$$E_x \frac{2\gamma^2(1-\cos\alpha)}{1+\gamma^2\theta^2+\frac{a_0^2}{2}+\gamma\frac{\lambda_c}{\lambda_0}}E_0. \tag{34}$$

In the low-energy limit (Thomson scattering), assuming that quantum and radiation reaction effects can be neglected, we can use a classical description and calculate the radiation spectrum for an ICS source with the same formalism as for betatron radiation, by calculating the electron trajectory and then using the radiation formula [Eq. (21)]. In this case, the undulator is not the plasma, but the counterpropagating laser pulse. Its undulator period and strength parameter are, respectively, $\lambda_u = \lambda_0/2$ and $K_u = a_0$, and the critical energy is (for $K_u \gg 1$):

$$E_c(\text{eV}) = 3K_u\gamma^2hc/\lambda_0. \tag{35}$$

The emitted number of photons, at mean energy $E \sim 0.3E_c$, follows the expression derived for betatron radiation [Eq. (31)]. For an electron beam with a number of electrons $N_e$ interacting with a laser pulse of power $P_L$ and length $\tau$, the total number of photons can be derived from the Compton scattering differential cross section,[49,50] which, in the laboratory frame, is

$$\frac{d\sigma}{d\theta} = \pi r_e \sin\theta\frac{1-\beta}{1+\beta}\left(\frac{E_x}{E_0}\right)^2\left(\frac{1-\beta\cos\theta}{1+\beta}\frac{E_x}{E_0} + \frac{1+\beta}{1-\beta\cos\theta}\frac{E_0}{E_x} - \frac{(1-\beta^2)(1-\cos^2\theta)}{(1-\beta\cos\theta)^2}\right), \tag{36}$$

where $r_e$ is the classical electron radius. Then, the number of photons emitted into a cone of angle $\theta_c$ is

$$N_x = 2\frac{N_eP_L\tau}{c\sigma_{xy}E_0}\sigma_c, \tag{37}$$

where $\sigma_{xy}$ is the electron beam area and $\sigma_c$ is the cross section integrated over the cone of angle $\theta_c$. While, in theory, the ICS spectrum can be monochromatic if the beam is observed within a small cone in the forward direction, its energy spread depends on the energy spread of the laser, electron beam energy and angular spread, and the observation angle subtended by the detector. The ICS spectrum energy spread is proportional to the interaction parameters as follows:[51]

$$\frac{\Delta E_x}{E_x} \propto \frac{\Delta E_0}{E_0} \propto 2\frac{\Delta\gamma}{\gamma} \propto -\gamma^2\Delta\varepsilon \propto -\frac{1}{4}\Delta\theta^2 \propto -\frac{\Delta a^2}{1+a^2}. \tag{38}$$

Here, the small angle $\varepsilon$ is different for each electron and represents the emittance of the electron beam and $a$ is the normalized vector potential across the laser beam. While the spectral width depends directly on the electron and laser energy spreads, it is also strongly affected by the electron beam emittance because of the $\gamma^2$ factor. Note that the negative variations are asymmetric broadening toward lower photon energies. Figure 5 shows this representative feature of inverse

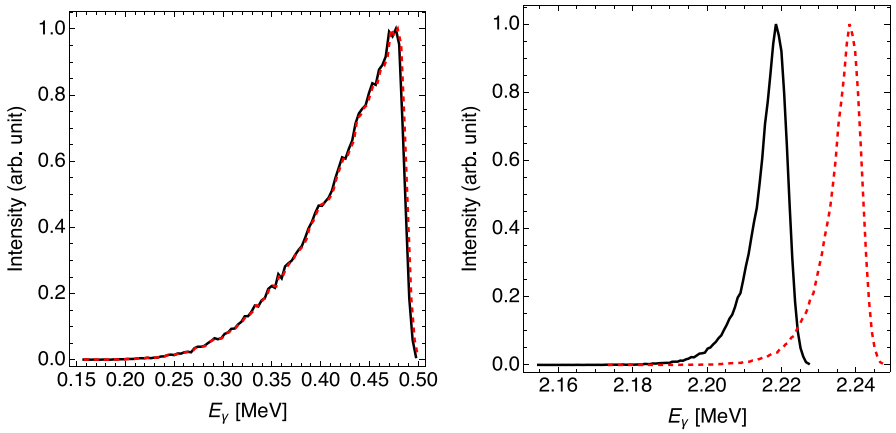


**FIG. 5.** X-ray spectra in the case of Compton scattering (black) and Thomson scattering (red) limits. Left parameters: scattering laser = 20 ps FWHM pulse duration, 532 nm wavelength, 34 $\mu$m rms spot size, 150 mJ; electron beam = 116 MeV, 40 $\mu$m rms spot size, 20 ps FWHM bunch length, 0.5 nC beam charge, 6 mm mrad normalized emittance. Right parameters: laser = 10 ps FWHM pulse duration, 532 nm wavelength, 12 $\mu$m rms spot size, 150 mJ; electron beam = 250 MeV, 15 $\mu$m rms spot size, 10 ps FWHM bunch length, 0.25 nC beam charge, 1 mm mrad normalized emittance. Reproduced with permission from Albert *et al.*, Phys. Rev. Spec. Top. Accel. Beams **14**, 050703 (2011); Copyright 2011 licensed under a Creative Commons Attribution (CC BY) license.[51]

Compton and Thomson scattering spectra for two different types of parameters and the signature of recoil.[51]

The theory of Compton scattering from the interaction of relativistic electrons with high intensity laser pulses has been well studied and includes cases such as nonlinear Thomson scattering theory for linearly or circularly polarized incident laser fields of arbitrary intensities and for electrons of arbitrary energies,[52,53] scattering pulses with very few cycles,[54] nonlinear effects producing broad spectral distributions of scattered photons with patterns of subpeaks,[55] or weakly nonlinear effects.[56] The idea of using LWFA for Compton scattering for high x-ray energies was originally proposed,[57] before being demonstrated with the scattering beam provided by a reflection of the drive beam off a plasma mirror[58] or by a secondary laser pulse.[59]

### C. Undulator and free electron laser

X-ray free electron lasers (XFELs) have been in operation for over a decade[60] and have since revolutionized many scientific fields by allowing the observation of ultrafast and ultrasmall phenomena.[61] Such facilities require kilometer-long accelerators to produce the GeV-class electrons necessary for their operation. As a result, there are very few of them in operation. XFELs using the self-amplified spontaneous emission (SASE) process include the Linac coherent light source (LCLS) in the USA, the European x-ray free electron laser (EuXFEL) in Germany, SACLA in Japan, and PAL-XFEL in Korea. These produce some of the brightest keV-class x rays on earth, with pulse energies of typically a few mj. Several groups have recently demonstrated that LWFA can now produce several GeV electron beams with PW-class laser systems and guiding,[62–64] comparable to what is needed for an XFEL, and thus, LWFA is being considered as a desirable approach to produce XFELs with a compact footprint. In 2021–2022, the field took a large step forward when a team demonstrated that it is possible to produce an XFEL with LWFA electrons,[7] which was followed by a demonstration of a seeded XFEL in the UV range.[8] Much progress has been made to produce LWFA beams with small emittances and large peak current; however, the large electron energy spread (a few %) is what currently limits LWFA-based XFELs. XFEL theory has been well studied analytically and with simulations[65] and can be understood by starting with the description of undulator radiation. For the betatron source, we have seen that electron motion is governed by longitudinal and transverse electrical fields [Eq. (14)]. For undulator radiation, the motion is governed by magnetic fields,

$$\frac{d\mathbf{p}}{dt} = -e(\mathbf{v} \times \mathbf{B}). \tag{39}$$

If we consider a planar undulator for which the magnetic field is in the vertical $y$ direction and varies sinusoidally along the $z$ (electron propagation) direction, such as $B_y = B_0 \cos(2\pi z/\lambda_u)$, then the electron transverse velocity is approximated by

$$v_x = \frac{K_u c}{\gamma} \sin\left(\frac{2\pi z}{\lambda_u}\right), \tag{40}$$

where $K_u = eB_0\lambda_u/2\pi mc = 0.934B_0$ (Tesla) $\lambda_u$ (cm) is the undulator strength. As for betatron radiation, because of transverse oscillations, the longitudinal velocity is only approximately equal to $c$. Assuming $\beta^2 = \beta_x^2 + \beta_z^2$, and the definition for $\gamma$ then the electron longitudinal velocity is

$$\beta_z = \frac{v_z}{c} = 1 - \frac{1 + K_u^2/2}{2\gamma^2} + \frac{K_u^2}{4\gamma^2}\cos 2k_u z \tag{41}$$

and the Lorentz contraction and relativistic Doppler shift with the modified relativistic factor $\gamma/(1 + K_u^2/2)$ yield the undulator equation describing the generation of x rays in the forward direction at the wavelength,

$$\lambda = \frac{\lambda_u}{2\gamma^2}\left(1 + \frac{K_u^2}{2} + \gamma^2\theta^2\right). \tag{42}$$

As the undulator strength increases beyond unity, harmonics of the fundamental radiation are emitted.

In an XFEL, the transverse motion of the electrons couples to the horizontal component of the radiation field, leading to energy transfer between the electrons to the radiation field. Depending on their phase with respect to the emitted wave, electrons either gain or lose energy, leading the electron beam to be microbunched with $\lambda$ periodicity and to consequently emit coherent radiation. When the wave gains energy, XFEL amplification occurs until saturation is reached. From Eq. (42), a spread in electron beam energy means a spread in $\lambda$, which prevents microbunching and, thus, XFEL gain. In a high gain FEL, the Pierce parameter[65]

$$\rho = \frac{1}{4\gamma}\left(\frac{I}{I_A}\frac{K_u^2[JJ]^2\lambda_u^2}{\pi^2\sigma_x^2}\right)^{1/3} \tag{43}$$

limits the acceptable electron beam energy spread $\sigma_\gamma$ to $\sigma_\gamma/\gamma \ll \rho$. Here, $I$ is the electron beam peak current, $I_A \sim 17$ kA is the Alfvén current, $\sigma_x$ is the *rms* beam size, and $[JJ] = J_0(Y) - J_1(Y)$ is the field coupling. $J_0$ and $J_1$ are Bessel functions and $Y = K_u^2/(4 + 2K_u^2)$.

Because current LWFA electron beam properties hardly satisfy the requirements for an XFEL, several undulator schemes have been numerically investigated to overcome the large energy spread of LWFA beams. A detailed discussion on this subject is presented in another Ref. 3. A transverse field variation into the FEL undulator reduces the effect of beam energy spread and jitter, and this method shows that it can produce soft x rays from 1 GeV electron beams with a 1% *rms* energy spread, for a 5 m long undulator with a periodicity of 1 cm.[66] Another concept has shown that FEL gain can be obtained for EUV rays with an electron beam energy spread of 1% *rms* and a bunch charge of 5 pC by using a large undulator strength $> 1$ and bunch decompression.[67] The electron energy considered was 300 MeV, and the FEL wavelength was calculated to $\lambda = 134$ nm. A chicane can also be used as a bunch stretcher,[68] which reduces the gain length for an XFEL operating with an energy spread on the order of the Pierce parameter. Space-charge effects due to the high peak beam currents (10–100 kA) of LWFAs are a problem as well. Solutions include the generation of electron beams with a negative energy chirp (the energy in the front of the beam is lower than at the tail) or the use of a tapered (variable period) undulator.[69] Thomson scattering was proposed as a method for conditioning FEL electron beams.[70] In this case, Thomson scattering of an intense focused laser pulse produces a correlation between the energy loss by an electron and its transverse location in the laser field.

For a long time, only undulator radiation had been produced, with 55–75 MeV, 1% energy spread electron beams in the visible wavelengths,[71] and with 200 MeV electron beams in the soft x-ray range, down to a few nm.[72] However, teams recently demonstrated lasing of a LWFA-driven XFELs at 27 and 270 nm (seeded) (Refs. 7 and 8). Transport quadrupoles and magnetic chicanes were necessary to properly shape the electron beam as it enters the undulator. A comparison between the results of this experiment and the performance of LCLS is shown in Fig. 6. Institutions worldwide continue to actively pursue the design of LFWA-driven XFELs.

### D. Bremsstrahlung

In a bremsstrahlung radiation source, high-energy electrons are converted into gamma-ray beams as they pass through a dense target. This process has been well investigated with conventional particle accelerators and is employed for flash-radiography systems. Bremsstrahlung sources from laser–plasma interaction experiments at relativistic intensities have been well studied, and in this case, the MeV electrons can be produced by various processes, including ponderomotive acceleration, direct laser acceleration, inverse bremsstrahlung, resonance absorption, or heating mechanisms. By comparing with these, LWFA produces electron beams with higher energies and lower emittances, which is attractive for applications requiring MeV-class photons, high flux, and small source sizes.

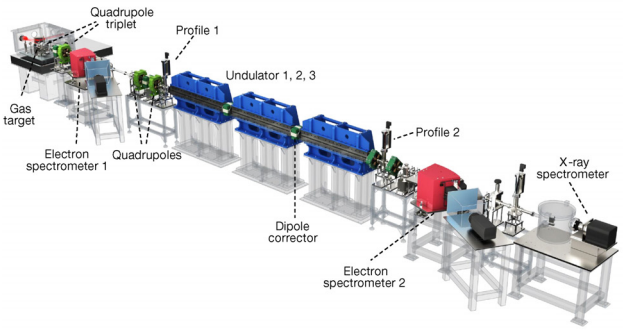


| Parameter | Wang et al | LCLS* |
|---|---|---|
| Energy (GeV) | 0.460 | 3.5-16.5** |
| Energy spread (%) | 0.5 | 0.1 |
| Energy fluctuation (%) | 3 | 0.02 |
| Charge (pC) | 30 | 180 |
| Peak Current (kA) | 5.7 | 1-5 |
| Divergence mrad | 0.2 | |
| Undulator period (cm) | 2.5 | 3 |
| Undulator strength | 1.41 | ~3.5 |
| FEL parameter | 0.005 | |
| Photon energy (eV) | 46 | 1000-25000 |
| Pulse energy (mJ) | $10^{-4}$ (av) | 0.6-2 |
| Energy fluctuation (%) | 54.2 | <10 |

* Hard x-rays 5 - 250 fs mode, LCLS user portal; **13.6 GeV for 8 keV x-rays

**FIG. 6.** Left: experimental setup used to produce a LWFA-driven XFEL and comparison between the experimental results and the LCLS parameters. Left figure reproduced with permission from Wang *et al.*, Nature **595**, 516–520 (2021) Copyright 2021 Springer.[7]

In a bremsstrahlung radiation source driven by LWFA, the relativistic electrons interact with the atoms of the high-Z converter target and produce high energy photons with energy $E_\gamma$. If we consider that the LWFA electrons interact with the solid target in the normal direction of the target surface, then they are slowed down and lose energy through processes, such as ionization, bremsstrahlung, and Ohmic heating. The photon energy distribution emitted at the back of the target is derived assuming a given electron energy distribution function inside the target, the bremsstrahlung cross section and the photoabsorption processes. If one assumes a differential cross section $d\sigma/dE_\gamma$, an electron mean free path $X_{el}$, a photon mean free path $X_{ph} = [\rho(\mu/\rho)]^{-1}$, and a mass absorption coefficient $\mu/\rho$, then a simplified expression for the on axis energy spectrum at the target backside emitted in the forward direction is[73]

$$\frac{d^2N_\gamma}{dE_\gamma d\Omega} = \frac{n_a N}{2\pi N_x}\int_{x=0}^{x_T} e^{\left[\frac{x_T-x}{X_{ph}}\right]}\left[\int_E^{E_{\max}} \frac{d\sigma}{dE_\gamma} e^{-\frac{E}{T}} \times e^{-\frac{x}{X_{el}}} dE\right] dx. \quad (44)$$

While not always exactly true for LWFA, this expression assumes a single-temperature hot electron Boltzmann energy distribution for simplicity. Here, $x_T$ is the solid target thickness, $n_a$ is its atomic density, $N$ and $N_x$ are the total number of electrons in the beam before interaction and at target depth $x$, $T$ is the electron distribution temperature, and $E_{max}$ is the maximum electron energy. In the relativistic regime, the total number of photons produced by bremsstrahlung in the target is

$$N_{ph} = N\sigma x_T n_a. \quad (45)$$

Finally, the angular distribution of the bremsstrahlung is a dipole field in the plane of the collision for a collision with a non-relativistic electron and is peaked in the direction of motion for a collision with a relativistic electron.

LWFA-driven bremsstrahlung sources have been first studied in the self-modulated regime.[74–76] Similar experiments were reproduced with a femtosecond laser system.[77] Electron beams (20–200 MeV), with Maxwellian temperatures around 40 MeV, interacting with a Tantalum converter, were used to produce gamma-rays with a small source size (320 $\mu$m) and low divergence (a few degrees). The source duration is expected to be on the order of the laser pulse duration (30 fs), and the photon dose is on the order of 1 Gy a few centimeters from the source. As a comparison, tumors are typically treated with photon doses on the order of 10's or Gy.

The source size can be as small as 30 $\mu$m with proper optimization of the electron beam parameters and using fs-class laser systems.[78] Approximately $10^8$ photons were generated in the 8–17 MeV gamma-ray region by 10–45 MeV LWFA electron beams produced with a 10 TW laser system and crossing a 2 mm Tantalum slab.[79] The yield of gamma-rays produced by LWFA electrons from a similar laser system exceeds the yield of gamma-rays from direct irradiation of solid targets by two orders of magnitude.[80] Progress made on LWFA electron beams now permits the production of tunable gamma-ray sources based on bremsstrahlung. A ~15 pC, 220 MeV, quasi-monoenergetic electron beam can produce $10^9$ photons around 10 MeV.[81] A 300 pC, 1 GeV, electron beam traversing a 1 mm Tungsten target would produce $6 \times 10^{11}$ photons/shot, with 0.1% of these having an energy greater than 15 MeV.

### E. Summary of x-ray sources properties

One of the principal advantages of x-ray sources driven by LWFA is their ability to cover a broad spectral range, which is particularly useful for applications. The exact performance of the sources is dictated by the laser and plasma parameters, and for a modest 50 TW laser system, betatron radiation, ICS, and Undulator radiation will produce photons with an average energy of 5 keV, 25 eV, and 650 keV, respectively,[3] with a number of photons/beam around $10^7 - 10^9$. Most of these sources are now routinely produced on laser systems with powers up to a few 100 TW, and Table I gives an overview of the most current properties, as observed experimentally. Figure 7 shows the ideal spectral range operation of each source, which current laser technology. A comparison of Betatron, ICS, and Bremsstrahlung radiation performed with the same electron beam parameters (a Maxwellian electron distribution extending up to about 300 MeV) can be found in Ref. 76. Therefore, betatron dominates for 1–20 keV, ICS for 20–200 keV, and Bremsstrahlung beyond 200 keV. With the establishment of specialized high power laser networks, such as LaserNetUS,[6] and the construction of new multi-PW laser systems, one can expect the photon energy and flux to be extended. High repetition rate laser technology, coupled with automation, will also improve the source repetition rate and stability.

## IV. OVERVIEW OF CURRENT APPLICATION TECHNIQUES

Comprehensive reviews of potential applications in biology, medicine, industry, defense, material, and high energy density science have been done elsewhere,[2,4,5] and here, we focus on three application techniques with which LWFA-driven sources have seen significant

**TABLE I.** Summary of experimental x-ray sources performance, with the best achievements to date. The table has been updated from Ref. 5 and reflects the range of source parameters that have been achieved at various facilities. For undulator radiation, the parameters are from Ref. 72 and for XFEL from Ref. 7.

| | Betatron | Compton | Bremsstrahlung | Undulator | XFEL |
|---|---|---|---|---|---|
| Energy range (eV) | $10^3$–$10^4$ | $10^3$–$10^7$ | $10^3$–$10^8$ | 170 | 46 |
| Bandwidth (%) | 100 | 50 | 100 | 22 | 2–7 |
| Number of photons | $10^9$ | $10^7$–$10^8$ | $10^8$ | $7 \times 10^4$ | $10^{10}$ |
| Source size ($\mu$m) | 1.8 | 1.5 | 320 | 270 | 2000 |
| Duration (fs) | $< 30$ | $< 30$ | $< 30$ | $< 30$ | $< 30$ |
| Collimation (mrad, fwhm) | 2.5 | 10 | 50 | 0.18 | ~0.5 |
| Repetition rate (Hz) | 10 | 10 | Limited by solid target | 10 | 1–5 |

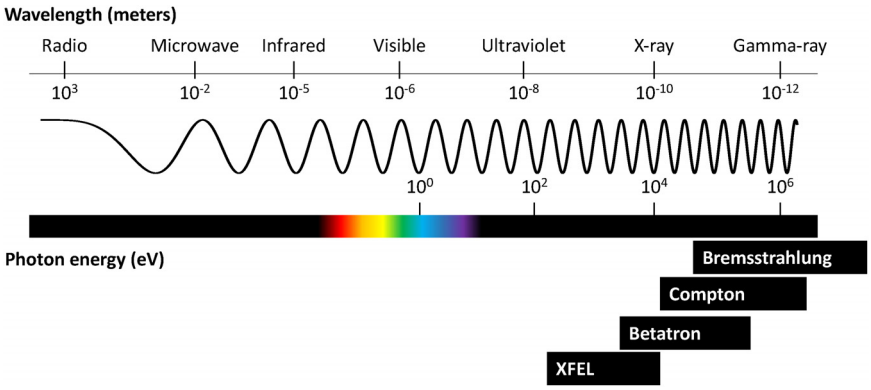


FIG. 7. Ideal spectral range operation of x-ray sources driven by LWFA.

progress in the past 5 years and are poised to have an impact. We also present some requirements necessary to take them to the next level.

### A. X-ray phase contrast imaging

Conventional x-ray radiography of objects relies on absorption contrast, which comes from density differences and variations in material composition and thickness. In materials where there is little absorption, such as soft biological tissue or carbon-based compounds, the radiography image contrast is very poor. In phase contrast imaging, contrast is obtained by phase variations in the transmitted beam, which arise from changes of the index of refraction. Phase contrast imaging is approximately a thousand times more sensitive than absorption contrast, but the advantage over absorption contrast will be more prominent in the hard x-ray region.[82]

When an x ray of wavelength $\lambda$ and wave vector $k$ propagates along the $z$ axis through a material with index of refraction $n = 1 - \delta - i\beta$, then the phase difference (compared to propagation through vacuum) is[83,84]

$$\phi(x,y) = -k\int_z \delta(x,y,z)dz = -\frac{2\pi r_e}{k}\int_z \rho(x,y,z)dz, \qquad (46)$$

where $r_e$ is the classical electron radius and $\rho$ is the electron density of the material. For x rays around 10 keV and low $Z$ material, $\delta \sim 10^{-6}$, and, hence, the angle of refraction is small. The 1D angle of propagation relative to the incident propagation direction is

$$\Delta\theta \sim \frac{1}{k}\frac{\partial\phi(x)}{\partial x}. \qquad (47)$$

Using x-ray phase contrast imaging requires good spatial coherence, which means a small effective source size. One way of achieving spatial transverse coherence without complex x-ray optics is to have a sufficiently small x-ray source size $w$ and let it diffract sufficiently at a distance $u$ away. By using x-ray projection microscopy in a scanning electron microscope (SEM), a spatial resolution of $< 0.2\,\mu$m has been demonstrated.[85] The spatial transverse coherence is defined by

$$L_c = \frac{\lambda u}{w}. \qquad (48)$$

X-ray sources driven by laser wakefield acceleration satisfy these requirements. For example, a betatron x-ray source with a 2 $\mu$m size, a critical energy $E_c = 8$ keV, and a source-object distance of 10 cm provides $L_c = 7.75\,\mu$m. Since only the spatial coherence of the x rays is important for forming the first peak of the interference pattern created between x rays that have accumulated different phase during propagation, XPCI can also be performed with broadband x rays.[83]

XPCI has been used in LWFA experiments for imaging biological samples, such as small animals[86–88] or bone samples.[89] Studies have demonstrated soft tissue phase contrast imaging and extraction of quantitative information by phase retrieval has also been performed,[90] and recent simulations show that it is possible to extend the resolution to the sub-micron regime.[91] Although betatron radiation is mostly employed, the inverse Compton source could also be used, and ICS with a conventional accelerator has been used for biological imaging.[92] Monoenergetic high energy x-ray sources are promising for this type of application because they can be tuned to maximize contrast at an absorption edge.[93] Applications are now expanding beyond biological and medical imaging and include imaging of surface defects in alloys,[94] inertial confinement fusion (ICF) capsules,[95,96] parts from additive manufacturing,[97] industrial imaging,[98] or the propagation of laser-driven shocks in high energy density matter.[99] Some examples are shown in Fig. 8.

These recent experiments are promising; however, some improvements are still necessary to make LWFA-based sources competitive for this application. To obtain quality images from XPCI, a sufficient number of photons $N_{ph}$ is necessary. Since x-ray CCDs used for these experiments are typically 1 Megapixels and the fluctuations from Poisson statistics scale with $1/\sqrt{n_{ij}}$, where $n_{ij}$ is the number of photons detected per pixel; then, we should have $N_{ph} \gg 10^6$ (assuming photons uniformly fill the detector). More photons are better, since the source is generally not uniform and the detection efficiency can be on order of a few %. In order to improve the quality of XPCI experiments with betatron radiation, future directions include repetition rate increase and a better field of view, currently limited to tens of mrad. Data acquisition rates of XPCI beam lines at synchrotrons are $> 10$ Hz and allow real-time visualization of internal physiological mechanisms. Current medical systems, as well as synchrotrons, have a field of view of $\sim$10 cm, whereas current betatron x-ray imaging experiments have a field of view of limited to about a cm, depending on magnification.

### B. High-energy, high-resolution radiography

Gamma-ray radiography is widely used for nondestructive evaluation[100,101] in a number of applications such as the inspection of cargo

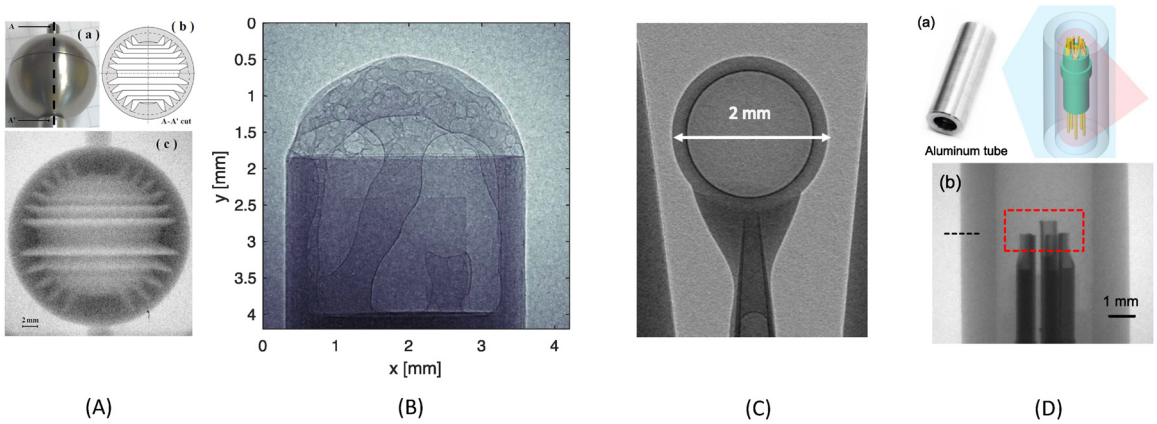


**FIG. 8.** Examples of imaging experiments done with LWFA-driven sources. (A) Tungsten image quality indicator (IQI) radiography with a bremsstrahlung source. Reproduced with permission from Ben-Ismail *et al.*, Nucl. Instrum. Methods Phys. Res. Sect. A **629**, 382–386 (2011). Copyright 2011 Elsevier.[78,109] (B) Phase contrast imaging of vacuum grease bubbling into vacuum with a betatron source of critical energy in the 2–5 keV range and size of 5 $\mu$m. Reproduced with permission from Vargas *et al.*, Plasma Phys. Controlled Fusion **61**, 054009 (2019). Copyright 2019 IOP Publishing.[97] (C) Phase contrast imaging of a 2 mm diameter capsule used in inertial confinement fusion experiments taken with a betatron source of critical energy around 15 keV and a source size $< 4$ $\mu$m. Reproduced with permission from Fourmaux *et al.* Opt. Express **28**, 13978–13990 (2020). Copyright 2020 Optica Publishing.[95] (D) Image of copper pins embedded in aluminum radiographed with an inverse Compton scattering source peaking at 100 keV and with a source size $< 14$ $\mu$m. Reproduced with permission from Ma *et al.*, Matter Radiat. Extremes **5**, 064401 (2020). Copyright 2020 AIP.[112]

containers or welded structures (pipes, vessels, tanks) produced by large industries. Compton scattering and bremsstrahlung from LWFAs present several advantages that are desired for this application: high energy photons (MeV) to penetrate dense objects, a low dose for safety, and a small source size (a few $\mu$m) for good spatial resolution.

Short pulse laser/solid interactions can directly produce gamma-rays suitable for radiography. High intensity laser pulses ($>10^{18}$ W/cm$^2$) are absorbed into hot electrons with a temperature on the order of the ponderomotive potential.[102] These hot electrons, observed in early experiments,[103,104] can produce copious amounts of gamma-rays with solid, high-Z targets, such as Gold or Tungsten.[105,106] At intensities of $10^{19}$ W/cm$^2$, $10^4$ photons/eV/Sr have been reported and were used to radiograph a high area density object (up to 85 g/cm$^3$).[106] The drawback is the rather large source size, about 400 $\mu$m, which limits the spatial resolution. Recent techniques, using shaped targets, such as compound parabolic concentrators,[107,108] have demonstrated yield improvement.

A better resolution can be achieved with bremsstrahlung produced by the interaction of LWFA electrons with a solid target in the self-modulated[74] and blowout[77] regime. The resolution in the first blowout regime experiment was 320 $\mu$m,[77] which was well improved to 30 $\mu$m with optimization of the electron beam parameters.[78,109]

Compton scattering is a promising source for this application, because of its potential tunability, narrow bandwidth, and small source size, when compared to bremsstrahlung. Gamma ray photons with energies up to 10 MeV and a spectral bandwidth of 10% have been measured for potential radiography applications.[110] In this experiment, using a driver for the electron beam and a scattering beam, the x-ray source size was measured to be 5 $\mu$m using a cross correlation technique in which the scattering pulse is scanned. In addition, the narrow divergence of the beam is well suited for long standoff imaging. A USB flash drive was radiographed with a 1.5 $\mu$m, 100 keV Compton scattering x-ray source,[58] with observation of very small features. For security applications, experiments have demonstrated that a 6–9 MeV Compton source can be used to detect concealed threats.[111] Figure 8 shows an example of imaging with a 100 keV inverse Compton source.

### C. Time-resolved x-ray absorption spectroscopy

The probing of high energy density (HED) conditions requires x rays to penetrate high density matter and helps to understand physics behind laser-driven fusion or the dynamics of planetary interiors, for example. In these conditions, physical processes, such as electron-ion equilibration, opacities, equations of state, continuum lowering, or non-thermal melting, happen over an ultrashort (sub-ps) time frame. Thus, x rays driven by LWFA are ideal for understanding these mechanisms through pump-probe experiments, where a sample is driven to an HED state by a driver (the pump) and probed by ultrafast x rays (the probe). In particular, the sub-ps duration of LWFA-driven light sources, their synchronization with a high intensity laser pulse and their broadband spectra are ideal for time-resolved x-ray absorption spectroscopy. X-ray absorption fine structure looks at the details of how x rays are absorbed by an element near the binding energies of the corresponding atom.[113] The absorption spectrum shows the modulations of the atom's x-ray absorption probability due to its chemical and physical state. It is sensitive to the oxidation state, coordination chemistry, the distances, coordination number, and species of the atoms immediately surrounding the selected element. Thus x-ray absorption fine structure determines the chemical state and local atomic structure for an atomic species and can be used in biology, materials science, catalysts studies, and high-energy density science. There are typically two regimes: x-ray absorption near-edge spectroscopy (XANES) and extended x-ray absorption fine-structure spectroscopy (EXAFS). XANES is generally within 30 eV of the absorption edge and provides information about electronic structures, while EXAFS is a couple 100 eV above the edge and provides geometric information. If the energy-dependent absorption coefficient of the

sample is $\mu(E) = log(I_0/I)$, where $I_0$ and $I$ are, respectively, the incident and transmitted x-ray intensities, then we define the EXAFS function as

$$\chi(E) = \frac{\mu(E) - \mu_0(E)}{\Delta\mu_0(E)}. \tag{49}$$

Here, $\mu_0(E)$ a smooth background as calculated in the absence of scattering, and $\Delta\mu_0(E)$ is the jump in absorption at the edge, located at energy $E_0$. In the EXAFS function, the energy is usually converted to $k = \sqrt{2m(E - E_0)/\hbar^2}$, the wave number of the photo electron, and the different frequencies in the oscillations can be described with the EXAFS equation:

$$\chi(k) = \sum_j \frac{N_j f_j(k) e^{-2k^2\sigma_j^2}}{kR_j^2} \sin\left[2kR_j + \sigma_j(k)\right], \tag{50}$$

where $f(k)$ and $\sigma(k)$ are the known scattering amplitude and phase-shift of the neighbor atoms to the excited atom, $N$ is the number of neighboring atoms, $R$ is the distance from the neighboring atom, and $\sigma_j^2$ is the mean square disorder in the distance for the $j$th shell. For context, the history of x-ray absorption spectroscopy and the derivation of Eq. (50) can be found in a review paper by Lytle.[114] Theoretical approaches to EXAFS and data inversion by the Fourier transform were first explained in Ref. 115 and reviewed in Ref. 113.

Using a sub-ps duration source for x-ray absorption spectroscopy is of potential great interest to study electron-ion equilibration processes in warm dense matter because the absorption spectrum allows retrieving the evolution of the ionization state $Z^*$, the electron temperature $T_e$, and the ion temperature $T_i$. Figure 9 illustrates this and shows x-ray absorption spectra for an aluminum sample at different temperature conditions. The evolution of the electron temperature has been measured with XANES in optically heated warm dense copper,[116] aluminum,[117] and iron.[118] Another class of experiments includes the study of various materials at Mbar pressures obtained from laser-driven shocks. In this case, x-ray diagnostic techniques can be either XANES,[119–122] or EXAFS.[123] Models used in these experiments can be improved with better temporal resolution, and, thus, several experiments have been performed using shorter duration synchrotron x rays to look at the electronic structure of warm dense copper and silicon dioxide. XANES experiments and XFEL probe have looked at shocked compressed matter, near the Molybdenum LIII edge (2.520 keV),[124] and the iron K-edge.[122] However, the stochastic nature of the SASE FEL spectrum makes this type of measurement extremely challenging.

Using betatron radiation for x-ray absorption spectroscopy in warm dense matter has been successfully attempted in several proof-of-principle experiments. A 200 TW laser was used to produce $10^6$ photons/eV betatron x rays in the 5 keV region, sufficient for XANES at the K-edge of a Titanium sample.[125] Another experiment used the source for XANES at the Copper L-edge, with about $10^5$ photons/eV at 1 keV, and >50 shot accumulations were necessary for the measurement.[126] For practical use as a user-facility-type source, the betatron source stability and flux still need to be improved. A successful XANES or EXAFS experiment needs to have a spectral resolution better than 2 eV. In general, the oscillation amplitude of the EXAFS signal is on the order of a few % of the total absorption signal (the edge step). Ideally, the random statistical noise, $SN = 1/\sqrt{N_{Ph}}$, where $N_{Ph}$ is the number of x-ray photons in the energy band of interest, should be 1/1000 of the EXAFS signal. This means that the condition $N_{Ph} > 10^6$/eV must be fulfilled to realize an EXAFS experiment with good statistics. The recent experiments[125,126] are around this threshold. The LWFA-driven betatron x-ray source should, in the near future, benefit from increased repetition rate laser systems and the emergence of PW-class laser user facilities. In addition to the quality of the x-ray source, instrumentation techniques (focusing, spectroscopy) can be specifically adapted for betatron x-ray radiation in order to achieve good spectral resolution.

## V. CONCLUSION AND OPEN QUESTIONS

X-ray sources driven by laser plasma acceleration are now well understood and enable unique new opportunities for applications. If one considers the four processes presented in this tutorial (betatron radiation, inverse Compton scattering, bremsstrahlung radiation, and undulator/XFEL radiation), these sources can produce tunable photons in the keV-MeV energy range, collimated beams (mrad), small source sizes ($\mu$m), and ultrashort pulse durations (fs-ps). Additionally, they are compact and can be synchronized with drive laser systems. Figure 10 shows a comparison of these sources with conventional light sources, adapted from a recent Ref. 5. Due to their properties, LWFA-driven light sources enable applications in medical, biological, and industrial imaging, radiography of dense objects, pump-probe experiments to understand transient phenomena and matter in extreme conditions by using absorption spectroscopy. With the emergence of modern high intensity laser facilities, such as the Extreme Light Infrastructure in Europe and open access high intensity laser networks

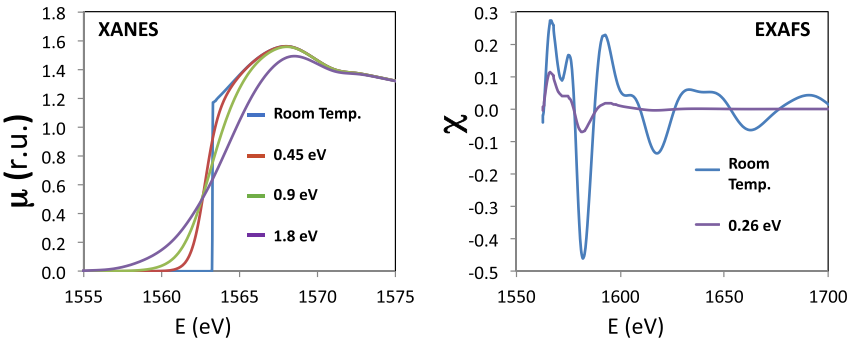


**FIG. 9.** XANES and EXAFS simulations (courtesy Y. Ping at LLNL) done with the FEFF code, an *ab initio* multiple-scattering code for calculating excitation spectra and electronic structure.[113,127] The simulations show the variation of the x-ray absorption spectrum for an aluminum sample near its K-edge, for different electron temperatures.

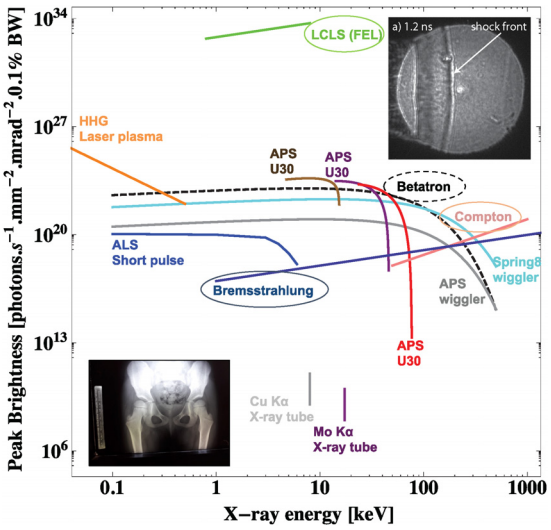


**FIG. 10.** Peak brightness of betatron, inverse Compton and bremsstrahlung radiation from LWFA compared with conventional light sources in the same energy range. Sources included in this plot are: The APS synchrotron U30 undulator (Argonne National Laboratory, USA), the ALS synchrotron (Lawrence Berkeley National Laboratory, USA), the Spring8 synchrotron (RIKEN, Japan), x-ray tubes (Copper and Molybdenum Kα), the LCLS free electron laser (SLAC, USA), and high harmonics generation from laser-produced plasmas. The images show a conventional radiograph from the author taken in the 1980s with an x-ray tube (bottom) and a phase contrast image of a laser-driven shock taken with the LCLS XFEL (top).[128] Reproduced with permission from Albert and Thomas, Plasma Phys. Controlled Fusion **58**, 103001 (2016). Copyright 2016 IOP Publishing.

such a LaserNetUS, we can expect to see many new developments in the coming years. Several open questions remain, among which, two important ones: First, will we ever have a portable, mini XFEL? Second, what will it take to make these sources practical for applications for users who want to use them without any background and expertise in laser-plasma physics?

A portable, mini-XFEL is likely, but not in the near future. Many improvements are still needed on the LWFA beam properties. First, higher electron energy is necessary to produce harder x rays than the recent demonstration at 27 nm.[7] The current highest energies produced by LWFA are reported at 8 GeV (5 pC),[62] 5 GeV,[63] and possibly 10 GeV.[129] Then, shot-to-shot electron beam energy stability will need to be improved by a factor of 10–100 for viable operation. Finally, the recent experiments, while a major breakthrough, demonstrated gain, but not full saturation.

In order to make these sources practical for applications, especially for communities not familiar with laser-plasma interaction experiments, several improvements are required, primarily source stability, and source flux. This will be made by the use of repetition rate technology, not only for the laser but also for the targets and diagnostics, and use of automation and machine learning to optimize source performance and data analysis, and accelerate the rate of discovery.[130,131] Steps in this direction are already taken for LWFA.[10] Ultimately, it will be the intersection of different communities with laser and plasma physicists that will drive innovation for applications of x-ray sources driven by laser wakefield acceleration.

## ACKNOWLEDGMENTS

This work was performed under the auspices of the U.S. Department of Energy under Contract No. DE-AC52-07NA27344 with support from the DOE Office of Science Early Career Research Program under No. SCW1575-1.

## AUTHOR DECLARATIONS

### Conflict of Interest

The author has no conflicts to disclose.

### Author Contributions

**Felicie Albert:** Investigation (equal); Writing – original draft (equal); Writing – review & editing (equal).

## DATA AVAILABILITY

Data sharing is not applicable to this article as no new data were created or analyzed in this study.

## REFERENCES

[1]T. Tajima and J. M. Dawson, "Laser electron accelerator," Phys. Rev. Lett. **43**, 267–270 (1979).
[2]F. Albert, M. E. Couprie, A. Debus, M. C. Downer, J. Faure, A. Flacco, L. A. Gizzi, T. Grismayer, A. Huebl, C. Joshi, M. Labat, W. P. Leemans, A. R. Maier, S. P. D. Mangles, P. Mason, F. Mathieu, P. Muggli, M. Nishiuchi, J. Osterhoff, P. P. Rajeev, U. Schramm, J. Schreiber, A. G. R. Thomas, J.-L. Vay, M. Vranic, and K. Zeil, "2020 roadmap on plasma accelerators," New J. Phys. **23**, 031101 (2021).
[3]S. Corde, K. T. Phuoc, G. Lambert, R. Fitour, V. Malka, and A. Rousse, "Femtosecond x rays from laser-plasma accelerators," Rev. Mod. Phys. **85**, 1–47 (2013).
[4]F. Albert, A. G. R. Thomas, S. P. D. Mangles, S. Banerjee, S. Corde, A. Flacco, M. Litos, D. Neely, J. Vieira, Z. Najmudin, R. Bingham, C. Joshi, and T. Katsouleas, "Laser wakefield accelerator based light sources: Potential applications and requirements," Plasma Phys. Controlled Fusion **56**, 084015 (2014).
[5]F. Albert and A. G. R. Thomas, "Applications of laser wakefield accelerator-based light sources," Plasma Phys. Controlled Fusion **58**, 103001 (2016).
[6]"Lasernetus website," information about the mission, facilities of LaserNetUS, and beam time allocation process can be found at https://lasernetus.org
[7]W. Wang, K. Feng, L. Ke, C. Yu, Y. Xu, R. Qi, Y. Chen, Z. Qin, Z. Zhang, M. Fang, J. Liu, K. Jiang, H. Wang, C. Wang, X. Yang, F. Wu, Y. Leng, J. Liu, R. Li, and Z. Xu, "Free-electron lasing at 27 nanometres based on a laser wakefield accelerator," Nature **595**, 516–520 (2021).
[8]M. Labat, J. C. Cabadağ, A. Ghaith, A. Irman, A. Berlioux, P. Berteaud, F. Blache, S. Bock, F. Bouvet, F. Briquez, Y.-Y. Chang, S. Corde, A. Debus, C. De Oliveira, J.-P. Duval, Y. Dietrich, M. El Ajjouri, C. Eisenmann, J. Gautier, R. Gebhardt, S. Grams, U. Helbig, C. Herbeaux, N. Hubert, C. Kitegi, O. Kononenko, M. Kuntzsch, M. LaBerge, S. Lê, B. Leluan, A. Loulergue, V. Malka, F. Marteau, M. H. N. Guyen, D. Oumbarek-Espinos, R. Pausch, D. Pereira, T. Püschel, J.-P. Ricaud, P. Rommeluere, E. Roussel, P. Rousseau, S. Schöbel, M. Sebdaoui, K. Steiniger, K. Tavakoli, C. Thaury, P. Ufer, M. Valléau, M. Vandenberghe, J. Vétéran, U. Schramm, and M.-E. Couprie, "Seeded free-electron laser driven by a compact laser plasma accelerator," Nat. Photonics **17**, 150–156 (2022).
[9]C. N. Danson, C. Haefner, J. Bromage, T. Butcher, J.-C. F. Chanteloup, E. A. Chowdhury, A. Galvanauskas, L. A. Gizzi, J. Hein, D. I. Hillier *et al.*, "Petawatt and exawatt class lasers worldwide," High Power Laser Sci. Eng. **7**, e54 (2019).
[10]S. Jalas, M. Kirchen, P. Messner, P. Winkler, L. Hübner, J. Dirkwinkel, M. Schnepp, R. Lehe, and A. R. Maier, "Bayesian optimization of a laser-plasma accelerator," Phys. Rev. Lett. **126**, 104801 (2021).

[11]E. Esarey, C. Schroeder, and W. P. Leemans, "Physics of laser-driven plasma-based electron accelerators," Rev. Mod. Phys. **81**, 1229 (2009).
[12]D. Strickland and G. Mourou, "Compression of amplified chirped optical pulses," Opt. Commun. **56**, 219 (1985).
[13]A. Siegman, *Lasers* (U. S. Books, 1986).
[14]L. V. Keldysh, "Ionization in the field of a strong electromagnetic wave," J. Exp. Theor. Phys. **20**, 1307–1314 (1965).
[15]P. Sprangle, C.-M. Tang, and E. Esarey, "Relativistic self-focusing of short-pulse radiation beams in plasmas," IEEE Trans. Plasma Sci. **15**, 145–153 (1987).
[16]P. Mora and T. M. Antonsen, "Electron cavitation and acceleration in the wake of an ultraintense, self-focused laser pulse," Phys. Rev. E **53**, R2068–R2071 (1996).
[17]P. Mora and T. M. Antonsen, Jr., "Kinetic modeling of intense, short laser pulses propagating in tenuous plasmas," Phys. Plasmas **4**, 217–229 (1997).
[18]P. Mora and F. Amiranoff, "Electron acceleration in a relativistic electron plasma wave," J. Appl. Phys. **66**, 3476–3481 (1989).
[19]A. Pak, K. A. Marsh, S. F. Martins, W. Lu, W. B. Mori, and C. Joshi, Phys. Rev. Lett. **104**, 025003 (2010).
[20]C. McGuffey, A. G. R. Thomas, W. Schumaker, T. Matsuoka, V. Chvykov, F. J. Dollar, G. Kalintchenko, V. Yanovsky, A. Maksimchuk, K. Krushelnick, V. Y. Bychenkov, I. V. Glazyrin, and A. V. Karpeev, Phys. Rev. Lett. **104**, 025004 (2010).
[21]J. Faure, C. Rechatin, A. Norlin, A. Lifschitz, Y. Glinec, and V. Malka, Nature **444**, 737 (2006).
[22]A. J. Gonsalves, K. Nakamura, C. Lin, D. Panasenko, S. Shiraishi, T. Sokollik, C. Benedetti, C. B. Schroeder, C. G. R. Geddes, J. van Tilborg, J. Osterhoff, E. Esarey, C. Toth, and W. P. Leemans, Nat. Phys. **7**, 862 (2011).
[23]C. Thaury, E. Guillaume, A. Lifschitz, K. Ta Phuoc, M. Hansson, G. Grittani, J. Gautier, J. P. Goddet, A. Tafzi, O. Lundh, and V. Malka, "Shock assisted ionization injection in laser-plasma accelerators," Sci. Rep. **5**, 16310 (2015).
[24]P. Mora, "Three-dimensional effects in the acceleration of test electrons in a relativistic electron plasma wave," J. Appl. Phys. **71**, 2087–2091 (1992).
[25]J. P. Palastro, J. L. Shaw, P. Franke, D. Ramsey, T. T. Simpson, and D. H. Froula, "Dephasingless laser wakefield acceleration," Phys. Rev. Lett. **124**, 134802 (2020).
[26]D. H. Froula, D. Turnbull, A. S. Davies, T. J. Kessler, D. Haberberger, J. P. Palastro, S.-W. Bahk, I. A. Begishev, R. Boni, S. Bucht, J. Katz, and J. L. Shaw, "Spatiotemporal control of laser intensity," Nat. Photonics **12**, 262–265 (2018).
[27]W. Lu, M. Tzoufras, C. Joshi, F. S. Tsung, W. B. Mori, J. Vieira, R. A. Fonseca, and L. O. Silva, "Generating multi-GeV electron bunches using single stage laser wakefield acceleration in a 3D nonlinear regime," Phys. Rev. Spec. Top. Acc. Beams **10**, 061301 (2007).
[28]A. Pukhov and J. Meyer-ter Vehn, "Relativistic laser-plasma interaction by multi-dimensional particle-in-cell simulations," Phys. Plasmas **5**, 1880–1886 (1998).
[29]S. P. D. Mangles, C. D. Murphy, Z. Najmudin, A. G. R. Thomas, J. L. Collier, A. E. Dangor, E. J. Divall, P. S. Foster, J. G. Gallacher, C. J. Hooker, D. A. Jaroszynski, A. J. Langley, W. B. Mori, P. A. Norreys, F. S. Tsung, R. Viskup, B. R. Walton, and K. Krushelnick, "Monoenergetic beams of relativistic electrons from intense laser-plasma interactions," Nature **431**, 535–538 (2004).
[30]C. G. R. Geddes, C. Toth, J. V. Tilborg, E. Esarey, C. B. Schroeder, D. Bruhwiler, C. Nieter, J. Cary, and W. P. Leemans, "High-quality electron beams from a laser wakefield accelerator using plasma-channel guiding," Nature **431**, 538–541 (2004).
[31]J. Faure, Y. Glinec, A. Pukhov, S. Kiselev, S. Gordienko, E. Lefebvre, J.-P. Rousseau, F. Burgy, and V. Malka, "A laser-plasma accelerator producing monoenergetic electron beams," Nature **431**, 541–544 (2004).
[32]A. Rousse, K. T. Phuoc, R. Shah, A. Pukhov, E. Lefebvre, V. Malka, S. Kiselev, F. Burgy, J.-P. Rousseau, D. Umstadter, and D. Hulin, "Production of a keV x-ray beam from synchrotron radiation in relativistic laser-plasma interaction," Phys. Rev. Lett. **93**, 135005 (2004).
[33]A. Modena, Z. Najmudin, A. E. Dangor, C. E. Clayton, K. A. Marsh, C. Joshi, V. Malka, C. B. Darrow, C. Danson, D. Neely, and F. N. Walsh, Nature **377**, 606 (1995).
[34]S. Kneip, S. R. Nagel, C. Bellei, N. Bourgeois, A. E. Dangor, A. Gopal, R. Heathcote, S. P. D. Mangles, J. R. Marquès, A. Maksimchuk, P. M. Nilson, K. T. Phuoc, S. Reed, M. Tzoufras, F. S. Tsung, L. Willingale, W. B. Mori, A. Rousse, K. Krushelnick, and Z. Najmudin, "Observation of synchrotron radiation from electrons accelerated in a Petawatt-laser-generated plasma cavity," Phys. Rev. Lett. **100**, 105006 (2008).
[35]F. Albert, N. Lemos, J. L. Shaw, B. B. Pollock, C. Goyon, W. Schumaker, A. M. Saunders, K. A. Marsh, A. Pak, J. E. Ralph, J. L. Martins, L. D. Amorim, R. W. Falcone, S. H. Glenzer, J. D. Moody, and C. Joshi, "Observation of betatron x-ray radiation in a self-modulated laser wakefield accelerator driven with picosecond laser pulses," Phys. Rev. Lett. **118**, 134801 (2017).
[36]C. Joshi, T. Tajima, J. M. Dawson, H. A. Baldis, and N. A. Ebrahim, "Forward Raman instability and electron acceleration," Phys. Rev. Lett. **47**, 1285–1288 (1981).
[37]E. Esarey, B. A. Shadwick, P. Catravas, and W. P. Leemans, "Synchrotron radiation from electron beams in plasma-focusing channels," Phys. Rev. E **65**, 056505 (2002).
[38]J. Jackson, *Classical Electrodynamics* (John Wiley and Sons, 1998).
[39]J. Larmor, "A dynamical theory of the electric and luminiferous medium—Part III: Relations with material media," Proc. R. Soc. London **61**, 272–285 (1897).
[40]A. Liénard, Eclairage Électr. **16**, 5 (1898).
[41]J. Schwinger, "On the classical radiation of accelerated electrons," Phys. Rev. **75**, 1912–1925 (1949).
[42]K. T. Phuoc, S. Corde, R. Shah, F. Albert, R. Fitour, J.-P. Rousseau, F. Burgy, B. Mercier, and A. Rousse, "Imaging electron trajectories in a laser-wakefield cavity using betatron x-ray radiation," Phys. Rev. Lett. **97**, 225002 (2006).
[43]K. Ta Phuoc, S. Corde, R. Fitour, R. Shah, F. Albert, J.-P. Rousseau, F. Burgy, A. Rousse, V. Seredov, and A. Pukhov, "Analysis of wakefield electron orbits in plasma wiggler," Phys. Plasmas **15**, 073106 (2008).
[44]J. Martins, S. Martins, R. Fonseca, and L. Silva, "Radiation post-processing in pic codes," Proc. SPIE **7359**, 73590V (2009).
[45]A. H. Compton, Phys. Rev. **21**, 483 (1923).
[46]F. Arutyunian and V. Tumanian, "The Compton effect on relativistic electrons and the possibility of obtaining high energy beams," Phys. Lett. **4**, 176–178 (1963).
[47]K. Chouffani, D. Wells, F. Harmon, J. Jones, and G. Lancaster, "Laser-Compton scattering from a 20 MeV electron beam," Nucl. Instrum. Methods Phys. Res. Sect. A **495**, 95–106 (2002).
[48]S. G. Rykovanov, C. G. R. Geddes, J.-L. Vay, C. B. Schroeder, E. Esarey, and W. P. Leemans, "Quasi-monoenergetic femtosecond photon sources from Thomson Scattering using laser plasma accelerators and plasma channels," J. Phys. B **47**, 234013 (2014).
[49]O. Klein and T. Nishina, "Über die Streuung von Strahlung durch freie Elektronen nach der neuen relativistischen Quantendynamik von Dirac," Z. Phys. **52**, 853–868 (1929).
[50]G. Bhatt, H. Grotch, E. Kazes, and D. A. Owen, "Relativistic spin-dependent Compton scattering from electrons," Phys. Rev. A **28**, 2195–2200 (1983).
[51]F. Albert, S. G. Anderson, D. J. Gibson, R. A. Marsh, S. S. Wu, C. W. Siders, C. P. J. Barty, and F. V. Hartemann, "Design of narrow-band Compton scattering sources for nuclear resonance fluorescence," Phys. Rev. Spec. Top. Accel. Beams **14**, 050703 (2011).
[52]E. Esarey, S. K. Ride, and P. Sprangle, "Nonlinear Thomson scattering of intense laser pulses from beams and plasmas," Phys. Rev. E **48**, 3003–3021 (1993).
[53]Y. Y. Lau, F. He, D. P. Umstadter, and R. Kowalczyk, "Nonlinear Thomson scattering: A tutorial," Phys. Plasmas **10**, 2155–2162 (2003).
[54]F. Mackenroth and A. Di Piazza, "Nonlinear Compton scattering in ultrashort laser pulses," Phys. Rev. A **83**, 032106 (2011).
[55]D. Seipt and B. Kämpfer, "Nonlinear Compton scattering of ultrashort intense laser pulses," Phys. Rev. A **83**, 022101 (2011).
[56]F. Albert, S. G. Anderson, D. J. Gibson, R. A. Marsh, C. W. Siders, C. P. J. Barty, and F. V. Hartemann, "Three-dimensional theory of weakly nonlinear Compton scattering," Phys. Plasmas **18**, 013108 (2011).
[57]F. V. Hartemann, D. J. Gibson, W. J. Brown, A. Rousse, K. T. Phuoc, V. Mallka, J. Faure, and A. Pukhov, "Compton scattering x-ray sources driven by

laser wakefield acceleration," Phys. Rev. Spec. Top. Accel. Beams **10**, 011301 (2007).
[58]K. T. Phuoc, S. Corde, C. Thaury, V. Malka, A. Tafzi, J. P. Goddet, R. C. Shah, S. Sebban, and A. Rousse, "All-optical Compton gamma-ray source," Nat. Photonics **6**, 308–311 (2012).
[59]N. D. Powers, I. Ghebregziabher, G. Golovin, C. Liu, S. Chen, S. Banerjee, J. Zhang, and D. P. Umstadter, Nat. Photonics **8**, 28–31 (2014).
[60]P. Emma, R. Akre, J. Arthur, R. Bionta, C. Bostedt, J. Bozek, A. Brachmann, P. Bucksbaum, R. Coffee, F.-J. Decker, Y. Ding, D. Dowell, S. Edstrom, A. Fisher, J. Frisch, S. Gilevich, J. Hastings, G. Hays, P. Hering, Z. Huang, R. Iverson, H. Loos, M. Messerschmidt, A. Miahnahri, S. Moeller, H.-D. Nuhn, G. Pile, D. Ratner, J. Rzepiela, D. Schultz, T. Smith, P. Stefan, H. Tompkins, J. Turner, J. Welch, W. White, J. Wu, G. Yocky, and J. Galayda, "First lasing and operation of an angstrom-wavelength free-electron laser," Nat. Photonics **4**, 641–647 (2011).
[61]C. Bostedt, S. Boutet, D. M. Fritz, Z. Huang, H. J. Lee, H. T. Lemke, A. Robert, W. F. Schlotter, J. J. Turner, and G. J. Williams, "Linac coherent light source: The first five years," Rev. Mod. Phys. **88**, 015007 (2016).
[62]A. J. Gonsalves, K. Nakamura, J. Daniels, C. Benedetti, C. Pieronek, T. C. H. de Raadt, S. Steinke, J. H. Bin, S. S. Bulanov, J. van Tilborg, C. G. R. Geddes, C. B. Schroeder, C. Tóth, E. Esarey, K. Swanson, L. Fan-Chiang, G. Bagdasarov, N. Bobrova, V. Gasilov, G. Korn, P. Sasorov, and W. P. Leemans, "Petawatt laser guiding and electron beam acceleration to 8 GeV in a laser-heated capillary discharge waveguide," Phys. Rev. Lett. **122**, 084801 (2019).
[63]B. Miao, J. E. Shrock, L. Feder, R. C. Hollinger, J. Morrison, R. Nedbailo, A. Picksley, H. Song, S. Wang, J. J. Rocca, and H. M. Milchberg, "Multi-GeV electron bunches from an all-optical laser wakefield accelerator," Phys. Rev. X **12**, 031038 (2022).
[64]K. Oubrerie, A. Leblanc, O. Kononenko, R. Lahaye, I. A. Andriyash, J. Gautier, J.-P. Goddet, L. Martelli, A. Tafzi, K. Ta Phuoc, S. Smartsev, and C. Thaury, "Controlled acceleration of GeV electron beams in an all-optical plasma waveguide," Light: Sci. Appl. **11**, 180 (2022).
[65]Z. Huang and K.-J. Kim, "Review of x-ray free-electron laser theory," Phys. Rev. Spec. Top. Accel. Beams **10**, 034801 (2007).
[66]Z. Huang, Y. Ding, and C. B. Schroeder, "Compact x-ray free-electron laser from a laser-plasma accelerator using a transverse-gradient undulator," Phys. Rev. Lett. **109**, 204801 (2012).
[67]A. R. Maier, A. Meseck, S. Reiche, C. B. Schroeder, T. Seggebrock, and F. Grüner, "Demonstration scheme for a laser-plasma-driven free-electron laser," Phys. Rev. X **2**, 031019 (2012).
[68]T. Seggebrock, A. R. Maier, I. Dornmair, and F. Grüner, "Bunch decompression for laser-plasma driven free-electron laser demonstration schemes," Phys. Rev. Spec. Top. Accel. Beams **16**, 070703 (2013).
[69]F. J. Grüner, C. B. Schroeder, A. R. Maier, S. Becker, and J. M. Mikhailova, "Space-charge effects in ultrahigh current electron bunches generated by laser-plasma accelerators," Phys. Rev. Spec. Top. Accel. Beams **12**, 020701 (2009).
[70]C. B. Schroeder, E. Esarey, and W. P. Leemans, "Electron-beam conditioning by Thomson scattering," Phys. Rev. Lett. **93**, 194801 (2004).
[71]H. P. Schlenvoigt, K. Haupt, A. Debus, F. Budde, O. Jackel, S. Pfotenhauer, H. Schwoerer, E. Rohwer, J. G. Gallacher, E. Brunetti, R. P. Shanks, S. M. Wiggins, and D. A. Jaroszynski, "A compact synchrotron radiation source driven by a laser-plasma wakefield accelerator," Nat. Phys. **4**, 130–133 (2008).
[72]M. Fuchs, R. Weingartner, A. Popp, Z. Major, S. Becker, J. Osterhoff, I. Cortrie, B. Zeitler, R. Hrlein, G. D. Tsakiris, U. Schramm, T. P. Rowlands-Rees, S. M. Hooker, D. Habs, F. Krausz, S. Karsch, and F. Grüner, "Laser-driven soft-X-ray undulator source," Nat. Phys. **5**, 826–829 (2009).
[73]A. Compant La Fontaine, C. Courtois, F. Gobet, F. Hannachi, J. R. Marquès, M. Tarisien, M. Versteegen, and T. Bonnet, "Bremsstrahlung spectrum and photon dose from short-pulse high-intensity laser interaction on various metal targets," Phys. Plasmas **26**, 113109 (2019).
[74]R. D. Edwards, M. A. Sinclair, T. J. Goldsack, K. Krushelnick, F. N. Beg, E. L. Clark, A. E. Dangor, Z. Najmudin, M. Tatarakis, B. Walton, M. Zepf, K. W. D. Ledingham, I. Spencer, P. A. Norreys, R. J. Clarke, R. Kodama, Y. Toyama, and M. Tampo, "Characterization of a gamma-ray source based on a laser-plasma accelerator with applications to radiography," Appl. Phys. Lett. **80**, 2129–2131 (2002).
[75]N. Lemos, F. Albert, J. L. Shaw, D. Papp, R. Polanek, P. King, A. L. Milder, K. A. Marsh, A. Pak, B. B. Pollock, B. M. Hegelich, J. D. Moody, J. Park, R. Tommasini, G. J. Williams, H. Chen, and C. Joshi, "Bremsstrahlung hard x-ray source driven by an electron beam from a self-modulated laser wakefield accelerator," Plasma Phys. Controlled Fusion **60**, 054008 (2018).
[76]N. Lemos, P. King, J. L. Shaw, A. L. Milder, K. A. Marsh, A. Pak, B. B. Pollock, C. Goyon, W. Schumaker, A. M. Saunders, D. Papp, R. Polanek, J. E. Ralph, J. Park, R. Tommasini, G. J. Williams, H. Chen, F. V. Hartemann, S. Q. Wu, S. H. Glenzer, B. M. Hegelich, J. Moody, P. Michel, C. Joshi, and F. Albert, "X-ray sources using a picosecond laser driven plasma accelerator," Phys. Plasmas **26**, 083110 (2019).
[77]Y. Glinec, J. Faure, L. L. Dain, S. Darbon, T. Hosokai, J. J. Santos, E. Lefebvre, J. P. Rousseau, F. Burgy, B. Mercier, and V. Malka, "High-resolution gamma-ray radiography produced by a laser-plasma driven electron source," Phys. Rev. Lett. **94**, 025003 (2005).
[78]A. Ben-Ismail, J. Faure, and V. Malka, "Optimization of gamma-ray beams produced by a laser-plasma accelerator," Nucl. Instrum. Methods Phys. Res. Sect. A **629**, 382–386 (2011).
[79]A. Giulietti, N. Bourgeois, T. Ceccotti, X. Davoine, S. Dobosz, P. D'Oliveira, M. Galimberti, J. Galy, A. Gamucci, D. Giulietti, L. A. Gizzi, D. J. Hamilton, E. Lefebvre, L. Labate, J. R. Marquès, P. Monot, H. Popescu, F. Réau, G. Sarri, P. Tomassini, and P. Martin, "Intense gamma ray source in the giant-dipole-resonance range driven by 10-TW laser pulses," Phys. Rev. Lett. **101**, 105002 (2008).
[80]Y. Oishi, T. Nayuki, A. Zhidkov, T. Fujii, and K. Nemoto, "Evaluation of yields of $\gamma$-rays produced by electrons from gas jets irradiated by low-energy laser pulses: Towards âvirtual radioisotopesâ," Jpn. J. Appl. Phys. **50**, 042702 (2011).
[81]S. Cipiccia, S. M. Wiggins, R. P. Shanks, M. R. Islam, G. Vieux, R. C. Issac, E. Brunetti, B. Ersfeld, G. H. Welsh, M. P. Anania, D. Maneuski, N. R. C. Lemos, R. A. Bendoyro, P. P. Rajeev, P. Foster, N. Bourgeois, T. P. A. Ibbotson, P. A. Walker, V. O. Shea, J. M. Dias, and D. A. Jaroszynski, "A tuneable ultra-compact high-power, ultra-short pulsed, bright gamma-ray source based on bremsstrahlung radiation from laser-plasma accelerated electrons," J. Appl. Phys. **111**, 063302 (2012).
[82]A. Momose, "Recent advances in x-ray phase imaging," Jpn. J. Appl. Phys. **44**, 6355–6367 (2005).
[83]S. Wilkins, T. E. Gureyev, D. Gao, A. Pogany, and A. W. Stevenson, "Phase contrast imaging using polychromatic hard x-rays," Nature **384**, 335 (1996).
[84]T. J. Davis, D. Gao, T. E. Gureyev, A. W. Stevenson, and S. W. Wilkins, "Phase-contrast imaging of weakly absorbing materials using hard x-rays," Nature **373**, 595–598 (1995).
[85]S. C. Mayo, P. R. Miller, S. W. Wilkins, T. J. Davis, D. Gao, T. E. Gureyev, D. Paganin, D. J. Parry, A. Pogany, and A. W. Stevenson, "Quantitative x-ray projection microscopy: Phase-contrast and multi-spectral imaging," J. Microsc. **207**, 79–96 (2002).
[86]S. Kneip, C. McGuffey, F. Dollar, M. S. Bloom, V. Chvykov, G. Kalintchenko, K. Krushelnick, A. Maksimchuk, S. P. D. Mangles, T. Matsuoka, Z. Najmudin, C. A. J. Palmer, J. Schreiber, W. Schumaker, A. G. R. Thomas, and V. Yanovsky, "X-ray phase contrast imaging of biological specimens with femtosecond pulses of betatron radiation from a compact laser plasma wakefield accelerator," Appl. Phys. Lett. **99**, 093701 (2011).
[87]S. Fourmaux, S. Corde, K. T. Phuoc, P. Lassonde, G. Lebrun, S. Payeur, F. Martin, S. Sebban, V. Malka, A. Rousse, and J. C. Kieffer, "Single shot phase contrast imaging using laser-produced betatron x-ray beams," Opt. Lett. **36**, 2426 (2011).
[88]Z. Najmudin, S. Kneip, M. S. Bloom, S. P. D. Mangles, O. Chekhlov, A. E. Dangor, A. Döpp, K. Ertel, S. J. Hawkes, J. Holloway, C. J. Hooker, J. Jiang, N. C. Lopes, H. Nakamura, P. A. Norreys, P. P. Rajeev, C. Russo, M. J. V. Streeter, D. R. Symes, and M. Wing, "Compact laser accelerators for x-ray phase-contrast imaging," Philos. Trans. R. Soc. London A **372**, 20130032 (2014).
[89]J. M. Cole, J. C. Wood, N. C. Lopes, K. Poder, R. L. Abel, S. Alatabi, J. S. J. Bryant, A. Jin, S. Kneip, K. Mecseki, D. R. Symes, S. P. D. Mangles, and Z. Najmudin, "Laser-wakefield accelerators as hard x-ray sources for 3D medical imaging of human bone," Sci. Rep. **5**, 13244 (2015).
[90]J. Wenz, S. Schleede, K. Khrennikov, M. Bech, P. Thibault, M. Heigoldt, F. Pfeiffer, and S. Karsch, "Quantitative x-ray phase-contrast microtomography from a compact laser-driven betatron source," Nat. Commun. **6**, 7568 (2015).

[91]J. van Tilborg, T. Ostermayr, H.-E. Tsai, T. Schenkel, C. G. R. Geddes, C. Schroeder, and E. Esarey, "Phase-contrast imaging with laser-plasma-accelerator betatron sources," Proc. SPIE **11886**, 118860Q (2021).
[92]P. Oliva, M. Carpinelli, B. Golosio, P. Delogu, M. Endrizzi, J. Park, I. Pogorelsky, V. Yakimenko, O. Williams, and J. Rosenzweig, "Quantitative evaluation of single-shot inline phase contrast imaging using an inverse Compton x-ray source," Appl. Phys. Lett. **97**, 134104 (2010).
[93]F. E. Carroll, "Tunable monochromatic x rays: A new paradigm in medicine," Am. J. Roentgenol. **179**, 583–590 (2002).
[94]A. E. Hussein, N. Senabulya, Y. Ma, M. J. V. Streeter, B. Kettle, S. J. D. Dann, F. Albert, N. Bourgeois, S. Cipiccia, J. M. Cole, O. Finlay, E. Gerstmayr, I. G. González, A. Higginbotham, D. A. Jaroszynski, K. Falk, K. Krushelnick, N. Lemos, N. C. Lopes, C. Lumsdon, O. Lundh, S. P. D. Mangles, Z. Najmudin, P. P. Rajeev, C. M. Schlepütz, M. Shahzad, M. Smid, R. Spesyvtsev, D. R. Symes, G. Vieux, L. Willingale, J. C. Wood, A. J. Shahani, and A. G. R. Thomas, "Laser-wakefield accelerators for high-resolution x-ray imaging of complex microstructures," Sci. Rep. **9**, 3249 (2019).
[95]S. Fourmaux, E. Hallin, A. Krol, J. L. Bourgade, and J. C. Kieffer, "X-ray phase contrast imaging of spherical capsules," Opt. Express **28**, 13978–13990 (2020).
[96]B. J. Kozioziemski, J. A. Koch, A. Barty, H. E. Martz, W.-K. Lee, and K. Fezzaa, "Quantitative characterization of inertial confinement fusion capsules using phase contrast enhanced x-ray imaging," J. Appl. Phys. **97**, 063103 (2005).
[97]M. Vargas, W. Schumaker, Z.-H. He, K. Behm, V. Chvykov, B. Hou, K. Krushelnick, A. Maksimchuk, J. A. Nees, V. Yanovsky, Z. Zhao, and A. G. R. Thomas, "X-ray phase contrast imaging of additive manufactured structures using a laser wakefield accelerator," Plasma Phys. Controlled Fusion **61**, 054009 (2019).
[98]J.-N. Gruse, M. Streeter, C. Thornton, C. Armstrong, C. Baird, N. Bourgeois, S. Cipiccia, O. Finlay, C. Gregory, Y. Katzir, N. Lopes, S. Mangles, Z. Najmudin, D. Neely, L. Pickard, K. Potter, P. Rajeev, D. Rusby, C. Underwood, J. Warnett, M. Williams, J. Wood, C. Murphy, C. Brenner, and D. Symes, "Application of compact laser-driven accelerator x-ray sources for industrial imaging," Nucl. Instrum. Methods Phys. Res. Sect. A **983**, 164369 (2020).
[99]J. C. Wood, D. J. Chapman, K. Poder, N. C. Lopes, M. E. Rutherford, T. G. White, F. Albert, K. T. Behm, N. Booth, J. S. J. Bryant, P. S. Foster, S. Glenzer, E. Hill, K. Krushelnick, Z. Najmudin, B. B. Pollock, S. Rose, W. Schumaker, R. H. H. Scott, M. Sherlock, A. G. R. Thomas, Z. Zhao, D. E. Eakins, and S. P. D. Mangles, "Ultrafast imaging of laser driven shock waves using betatron x-rays from a laser wakefield accelerator," Sci. Rep. **8**, 11010 (2018).
[100]P. Reimers, J. Goebbels, H.-P. Weise, and K. Wilding, "Some aspects of industrial non-destructive evaluation by x- and gamma-ray computed tomography," Nucl. Instrum. Methods Phys. Res. **221**, 201–206 (1984).
[101]D. S. P. S. H. Martz and C. M. Logan, *X-Ray Imaging, Fundamentals, Industrial Techniques, and Applications* (CRC Press, 2016).
[102]S. C. Wilks, W. L. Kruer, M. Tabak, and A. B. Langdon, "Absorption of ultra-intense laser pulses," Phys. Rev. Lett. **69**, 1383–1386 (1992).
[103]P. Gibbon, "Efficient production of fast electrons from femtosecond laser interaction with solid targets," Phys. Rev. Lett. **73**, 664–667 (1994).
[104]G. Malka and J. L. Miquel, "Experimental confirmation of ponderomotive-force electrons produced by an ultrarelativistic laser pulse on a solid target," Phys. Rev. Lett. **77**, 75–78 (1996).
[105]M. D. Perry, J. A. Sefcik, T. Cowan, S. Hatchett, A. Hunt, M. Moran, D. Pennington, R. Snavely, and S. C. Wilks, "Hard x-ray production from high intensity laser solid interactions (invited)," Rev. Sci. Instrum. **70**, 265–269 (1999).
[106]C. Courtois, R. Edwards, A. Compant La Fontaine, C. Aedy, S. Bazzoli, J. L. Bourgade, J. Gazave, J. M. Lagrange, O. Landoas, L. L. Dain, D. Mastrosimone, N. Pichoff, G. Pien, and C. Stoeckl, "Characterisation of a MeV Bremsstrahlung x-ray source produced from a high intensity laser for high areal density object radiography," Phys. Plasmas **20**, 083114 (2013).
[107]D. R. Rusby, P. M. King, A. Pak, N. Lemos, S. Kerr, G. Cochran, I. Pagano, A. Hannasch, H. Quevedo, M. Spinks, M. Donovan, A. Link, A. Kemp, S. C. Wilks, G. J. Williams, M. J.-E. Manuel, Z. Gavin, A. Haid, F. Albert, M. Aufderheide, H. Chen, C. W. Siders, A. Macphee, and A. Mackinnon, "Enhancements in laser-generated hot-electron production via focusing cone targets at short pulse and high contrast," Phys. Rev. E **103**, 053207 (2021).
[108]P. King, D. Rusby, A. Hannasch, N. Lemos, G. Tiwari, A. Pak, S. Kerr, G. Cochran, I. Pagano, G. Williams, S. Khan, M. Aufderheide, A. Kemp, S. Wilks, A. Macphee, F. Albert, B. Hegelich, M. Downer, M. Manuel, Z. Gavin, A. Haid, and A. Mackinnon, "Enhancement of high energy x-ray radiography using compound parabolic concentrator targets," High Energy Density Phys. **42**, 100978 (2022).
[109]A. Ben-Ismail, O. Lundh, C. Rechatin, J. K. Lim, J. Faure, S. Corde, and V. Malka, "Compact and high-quality gamma-ray source applied to 10 $\mu$m-range resolution radiography," Appl. Phys. Lett. **98**, 264101 (2011).
[110]S. Banerjee, S. Chen, N. Powers, D. Haden, C. Liu, G. Golovin, J. Zhang, B. Zhao, S. Clarke, S. Pozzi, J. Silano, H. Karwowski, and D. Umstadter, "Compact source of narrowband and tunable x-rays for radiography," Nucl. Instrum. Methods Phys. Res. Sect. B **350**, 106–111 (2015).
[111]S. Chen, G. Golovin, C. Miller, D. Haden, S. Banerjee, P. Zhang, C. Liu, J. Zhang, B. Zhao, S. Clarke, S. Pozzi, and D. Umstadter, "Shielded radiography with a laser-driven MeV-energy x-ray source," Nucl. Instrum. Methods Phys. Res. Sect. B **366**, 217–223 (2016).
[112]Y. Ma, J. Hua, D. Liu, Y. He, T. Zhang, J. Chen, F. Yang, X. Ning, Z. Yang, J. Zhang, C.-H. Pai, Y. Gu, and W. Lu, "Region-of-interest micro-focus computed tomography based on an all-optical inverse Compton scattering source," Matter Radiat. Extremes **5**, 064401 (2020).
[113]J. J. Rehr and R. C. Albers, "Theoretical approaches to x-ray absorption fine structure," Rev. Mod. Phys. **72**, 621–654 (2000).
[114]F. W. Lytle, "The EXAFS family tree: A personal history of the development of extended X-ray absorption fine structure," J. Synchrotron Radiat. **6**, 123–134 (1999).
[115]D. E. Sayers, E. A. Stern, and F. W. Lytle, "New technique for investigating noncrystalline structures: Fourier analysis of the extended x-ray—Absorption fine structure," Phys. Rev. Lett. **27**, 1204–1207 (1971).
[116]B. I. Cho, K. Engelhorn, A. A. Correa, T. Ogitsu, C. P. Weber, H. J. Lee, J. Feng, P. A. Ni, Y. Ping, A. J. Nelson, D. Prendergast, R. W. Lee, R. W. Falcone, and P. A. Heimann, Phys. Rev. Lett. **106**, 167601 (2011).
[117]F. Dorchies, A. Levy, C. Goyon, P. Combis, D. Descamps, C. Fourment, M. Harmand, S. Hulin, P. M. Leguay, S. Petit, O. Peyrusse, and J. J. Santost, Phys. Rev. Lett. **107**, 245006 (2011).
[118]A. Fernandez-Pañella, T. Ogitsu, K. Engelhorn, A. A. Correa, B. Barbrel, S. Hamel, D. G. Prendergast, D. Pemmaraju, M. A. Beckwith, L. J. Bae, J. W. Lee, B. I. Cho, P. A. Heimann, R. W. Falcone, and Y. Ping, "Reduction of electron-phonon coupling in warm dense iron," Phys. Rev. B **101**, 184309 (2020).
[119]A. Levy, F. Dorchies, A. Benuzzi-Mounaix, A. Ravasio, F. Festa, V. Recoules, O. Peyrusse, N. Amadou, E. Brambrink, T. Hall, M. Koenig, and S. Mazevet, Phys. Rev. Lett. **108**, 055002 (2012).
[120]A. Benuzzi-Mounaix, F. Dorchies, V. Recoules, F. Festa, O. Peyrusse, A. Levy, A. Ravasio, T. Hall, M. Koenig, N. Amadou, E. Bambrink, and S. Mazevet, "Electronic structure investigation of highly compressed aluminum with *K*-edge absorption spectroscopy," Phys. Rev. Lett. **107**, 165006 (2011).
[121]J. Gaudin, C. Fourment, B. I. Cho, K. Engelhorn, E. Galtier, M. Harmand, P. M. Leguay, H. J. Lee, B. Nagler, M. Nakatsutsumi, C. Ozkan, M. Störmer, S. Toleikis, T. Tschentscher, P. A. Heimann, and F. Dorchies, "Towards simultaneous measurements of electronic and structural properties in ultra-fast x-ray free electron laser absorption spectroscopy experiments," Sci. Rep. **4**, 4724 (2014).
[122]M. Harmand, A. Ravasio, S. Mazevet, J. Bouchet, A. Denoeud, F. Dorchies, Y. Feng, C. Fourment, E. Galtier, J. Gaudin, F. Guyot, R. Kodama, M. Koenig, H. J. Lee, K. Miyanishi, G. Morard, R. Musella, B. Nagler, M. Nakatsutsumi, N. Ozaki, V. Recoules, S. Toleikis, T. Vinci, U. Zastrau, D. Zhu, and A. Benuzzi-Mounaix, "X-ray absorption spectroscopy of iron at multimegabar pressures in laser shock experiments," Phys. Rev. B **92**, 024108 (2015).
[123]Y. Ping, F. Coppari, D. G. Hicks, B. Yaakobi, D. E. Fratanduono, S. Hamel, J. H. Eggert, J. R. Rygg, R. F. Smith, D. C. Swift, D. G. Braun, T. R. Boehly, and G. W. Collins, Phys. Rev. Lett. **111**, 065501 (2013).
[124]F. Dorchies, F. Festa, V. Recoules, O. Peyrusse, A. Benuzzi-Mounaix, E. Brambrink, A. Levy, A. Ravasio, M. Koenig, T. Hall, and S. Mazevet, "X-ray absorption *K* edge as a diagnostic of the electronic temperature in warm dense aluminum," Phys. Rev. B **92**, 085117 (2015).

[125]B. Kettle, E. Gerstmayr, M. J. V. Streeter, F. Albert, R. A. Baggott, N. Bourgeois, J. M. Cole, S. Dann, K. Falk, I. Gallardo González, A. E. Hussein, N. Lemos, N. C. Lopes, O. Lundh, Y. Ma, S. J. Rose, C. Spindloe, D. R. Symes, M. Šmíd, A. G. R. Thomas, R. Watt, and S. P. D. Mangles, "Single-shot multi-keV x-ray absorption spectroscopy using an ultrashort laser-wakefield accelerator source," Phys. Rev. Lett. **123**, 254801 (2019).
[126]B. Mahieu, N. Jourdain, K. Ta Phuoc, F. Dorchies, J. P. Goddet, A. Lifschitz, P. Renaudin, and L. Lecherbourg, "Probing warm dense matter using femtosecond x-ray absorption spectroscopy with a laser-produced betatron source," Nat. Commun. **9**, 3276 (2018).
[127]J. J. Rehr, J. J. Kas, M. P. Prange, A. P. Sorini, Y. Takimoto, and F. Vila, "*Ab initio* theory and calculations of x-ray spectra," C. R. Phys. **10**, 548–559 (2009).
[128]A. Schropp, R. Hoppe, V. Meier, J. Patommel, F. Seiboth, Y. Ping, D. G. Hicks, M. A. Beckwith, G. W. Collins, A. Higginbotham, J. S. Wark, H. J. Lee, B. Nagler, E. C. Galtier, B. Arnold, U. Zastrau, J. B. Hastings, and C. G. Schroer, "Imaging shock waves in diamond with both high temporal and spatial resolution at an XFEL," Sci. Rep. **5**, 11089 (2015).
[129]C. Aniculaesei, T. Ha, S. Yoffe, E. McCary, M. M. Spinks, H. J. Quevedo, L. Labun, O. Z. Labun, R. Sain, A. Hannasch, R. Zgadzaj, I. Pagano, J. A. Franco-Altamirano, M. L. Ringuette, E. Gaul, S. V. Luedtke, G. Tiwari, B. Ersfeld, E. Brunetti, H. Ruhl, T. Ditmire, S. Bruce, M. E. Donovan, D. A. Jaroszynski, M. C. Downer, and B. M. Hegelich, "High-charge 10 GeV electron acceleration in a 10 cm nanoparticle-assisted hybrid wakefield accelerator," arXiv:2207.11492 (2022).
[130]T. Ma, D. Mariscal, R. Anirudh, T. Bremer, B. Z. Djordjevic, T. Galvin, E. Grace, S. Herriot, S. Jacobs, B. Kailkhura, R. Hollinger, J. Kim, S. Liu, J. Ludwig, D. Neely, J. J. Rocca, G. G. Scott, R. A. Simpson, B. S. Spears, T. S. Spinka, K. Swanson, J. J. Thiagarajan, B. V. Essen, S. Wang, S. C. Wilks, G. J. Williams, J. Zhang, M. C. Herrmann, and C. Haefner, "Accelerating the rate of discovery: Toward high-repetition-rate HED science," Plasma Phys. Controlled Fusion **63**, 104003 (2021).
[131]P. V. Heuer, S. Feister, D. B. Schaeffer, and H. G. Rinderknecht, "Preface to special topic: The high repetition rate frontier in high-energy-density physics," Phys. Plasmas **29**, 110401 (2022).